Los Alamos
NATIONAL LABORATORY
EST.1943

LA-UR-14-27296
Approved for public release; distribution is unlimited.

Title: Report on casting modeling and simulation

Author(s): Unal, Cetin
Carlson, Neil N.

Intended for: DOE Deliverable

Issued: 2014-09-18

Disclaimer:
Los Alamos National Laboratory, an affirmative action/equal opportunity employer,is operated by the Los Alamos National Security, LLC for the National NuclearSecurity Administration of the U.S. Department of Energy under contract DE-AC52-06NA25396. By approving this article, the publisher recognizes that the U.S. Government retains nonexclusive, royalty-free license to publish or reproduce the published form of this contribution, or to allow others to do so, for U.S. Government purposes. Los Alamos National Laboratory requests that the publisher identify this article as work performed under the auspices of the U.S. Departmentof Energy. Los Alamos National Laboratory strongly supports academic freedom and a researcher's right to publish; as an institution, however, the Laboratory does not endorse the viewpoint of a publication or guarantee its technical correctness.

Appendix E
FCT Document Cover Sheet

Name/Title of Deliverable/Milestone	Report on casting modeling and simulations
Work Package Title and Number	M3FT-14LA0204041
Work Package WBS Number	FT-14LA020404
Responsible Work Package Manager	Cetin Unal (Name/Signature)

Date Submitted 9/15/2014

Quality Rigor Level for Deliverable/Milestone ☒ -QRL-3 ☐ QRL-2 ☐ QRL-1 ☐ N/A* ☐ Nuclear Data

This deliverable was prepared in accordance with LANL
(Participant/National Laboratory Name)

QA program which meets the requirements of
☒ - DOE Order 414.1 ☐ NQA-1-2000 ☐ Other

This Deliverable was subjected to:

☒ Technical Review ☐ Peer Review

Technical Review (TR)

Review Documentation Provided

☐ Signed TR Report or,
☐ Signed TR Concurrence Sheet or,
☒ Signature of TR Reviewer(s) below

Peer Review (PR)

Review Documentation Provided

☐ Signed PR Report or,
☐ Signed PR Concurrence Sheet or,
☐ Signature of PR Reviewer(s) below

Name and Signature of Reviewers

Pratap Sadasivan

*NOTE *In some cases there may be a milestone where an item is being fabricated, maintenance is being performed on a facility, or a document is being issued through a formal document control process where it specifically calls out a formal review of the document. In these cases, documentation (e.g., inspection report, maintenance request, work planning package documentation or the documented review of the issued document through the document control process) of the completion of the activity along with the Document Cover Sheet is sufficient to demonstrate achieving the milestone. QRL for such milestones may also be marked N/A in the work package provided the work package clearly specifies the requirement to use the Document Cover Sheet and provide supporting documentation.*

Report on casting modeling and simulation

Prepared by

Cetin Unal and Neil Carlson

Los Alamos National Laboratory

Los Alamos, NM 87544

Summary

New modeling capabilities needed to simulate the casting of metallic fuels are added to Truchas code. In this report we summarize improvements we made in 2014 in three areas; 1- the implementation of an adiabatic gas bubble model into Truchas to model liquid-gas flow, 2- the implementation of surface tension model into Truchas for unstructured mesh required to run U-Zr casting, 3-the simulation of INL's U-Zr casting experiments with Flow3D computer program.

An alternative modeling approach for liquid-gas flow has been implemented. The new gas bubble method is intended for large multi-phase flow calculations, where a phase (i.e., material) can be designated as void (e.g., gas bubbles), whose detailed velocity and pressure are of no interest, only its effect on the surrounding fluid flow. The method uses an adiabatic relation between the bubble volumes and pressures to compute the effect of bubbles on the surrounding flow and only solves the flow equations in the fluid (and not inside the bubbles). Compared to the existing fluid flow algorithm, the new bubble model treats bubbles as compressible. While the algorithm is demonstrated to work for simple test cases, much more testing and validation are required to ensure robustness and production quality

Surface tension effects occur at an interface of two fluids when modeling multiphase flow. The earlier generalization of surface tension considered this effect acting as a tensile force on an interface. With the introduction of the continuum surface force (CSF) formulation this effect has been interpreted as volumetric force acting over the interface thickness.

Truchas casting code has surface tension models, which utilize convolution-based algorithms based on Rudman kernels and Willams kernels. The convolution algorithm requires a localized computation of the component volume fractions in the nearby cells to the interface. Such computations can be prohibitively

expensive in parallel and engender load-balancing issues where one processor is computing the convolution integral and others await the results from such evaluations. This problem arises further due to poor scalability of the convolution algorithm used currently. Another issue with the convolution-based algorithm is the Williams kernel that utilizes an eighth order kernel has an abrupt change in the heavy side function from 0 to 1.0 and consequently poor approximation properties of the gradients and curvatures. In comparison Rudman kernels have performed better which only utilize the sixth order kernel and has been found to be suitable for solving problems. Also applicability of the convolution algorithms (either Williams or Rudman) on unstructured meshes have been limited because of the lack of appropriate interpretations of the radius of curvature required in the convolution process.

We identified and prototyped a scalable FE-based smoothing procedure that in early testing looks to be a very promising replacement for the existing non-scalable convolution algorithm. Separately, we have developed a FE-based scheme for calculating curvatures. This has the potential for capturing contact angle physics, but that has not yet been seriously investigated. This scheme has also not yet been coupled to the new smoothing procedure. Much work remains to be done to further verification of the new smoothing procedure, modeling contact angle and production-quality implementation.

Computational simulations of gravity casting for metallic U-Zr nuclear fuel rods were performed with the flow solver Flow3d. Numerical simulations were validated with experimental data obtained by Idaho National Laboratory (INL). The experimentally measured transient temperature profiles inside the casting apparatus were matched by adjusting primarily the heat transfer coefficients between melt and mold at different locations. The volume of the rods cast, length of rods were predicted through the transient casting process and were found to be in a reasonable agreement with experimental data. A sensitivity analysis with vent locations, pressure, mesh refinement and effects of the surface tension at the interface was explored. This paper provides specific guidelines on using numerical experiments for better understanding of the gravity casting process. This work serves as a validation benchmark for the casting problem and provides guidelines when performing simulation exercises for modeling casting. The validated modeling parameters will be used in the simulation of larger size caster with larger outputs in the coming fiscal year.

Below we present the details of improvements and achievements in each area. The primary author who did the work is listed in each section.

New flow physics: Adiabatic bubble model

by

Jozsef Bakosi

A new flow physics option, the adiabatic bubble model, has been implemented in Truchas. This is similar to the "homogeneous bubble model" option available in Flow3D. The rationale behind such a bubble model is two-fold: (1) to speed up and make large multi-phase-flow calculations more robust that involve many gas bubbles where the flow field inside the bubbles is of no interest, and (2) to more accurately approximate the underlying physics, as the gas density in such calculations may be orders of magnitude smaller than the liquid and compressible, compared to the existing flow algorithm which treats materials as incompressible.

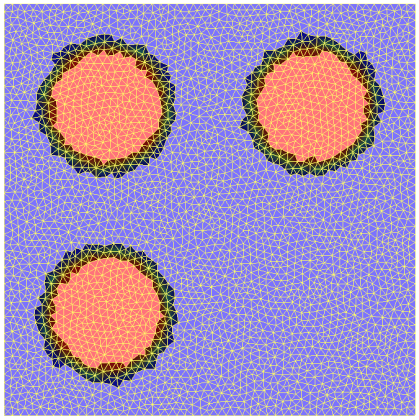


Figure 1. Three bubbles surrounded by liquid. The bubble model does not solve the flow quations inside the bubbles.

Overview

Figure 1. Illustrates three bubbles surrounded by liquid with an overlaid 2D triangular computational mesh. Note that the figure is only an illustration -- the algorithm in Truchas works with 3D cells. In the bubble model the mesh cells and nodes inside the red circular bubbles do not participate in the solution of the flow. Instead, the bubble pressures are assumed homogeneous and influence the surrounding liquid by exerting a force due to changes in the bubble volumes.

Based on designating a material as void, by assigning zero density, bubbles are identified and tracked throughout the evolution of the flow field in space and time. Instead of integrating the flow equations inside bubbles, their pressures are governed by the relation

$$p = p_0 \left(\frac{V_0}{V}\right)^{\gamma},$$

where p and p_0 denote the current-, and previous-time bubble pressures, V and V_0 are the current and

previous-time bubble volumes, respectively, and γ is the ratio of specific heats. Each bubble is assigned its initial pressure specified by the user via the input deck. The initial bubble volumes are computed based on the geometrical layout of the void material (designated as bubbles by assigning zero density) in the input deck. The bubble volumes and pressures evolve in time due to forces by the surrounding liquid (or gas) flow computed by the existing fluid flow algorithm in Truchas.

As the above equation shows, the bubble model neglects heat transfer inside bubbles, but assumes that the bubbles are compressible. The computed bubble pressure affects the surrounding fluid via enforcing the bubble pressure on the surface between the bubble and the fluid.

Bubble model algorithm

To compute the influence of the changing bubble pressures on the surrounding-fluid pressure, the bubble model algorithm needs to be able to identify distinct bubbles on a computational mesh. It also needs to track current and previous bubble volumes between time steps. Additionally, bubbles can split and merge, so the algorithm needs be able to maintain the relationship between splitting and merging bubbles as time evolves. Finally, to be practically useful for large problems, the algorithm must work with bubbles crossing processing element (PE) boundaries. In the following some aspects of the above requirements are detailed.

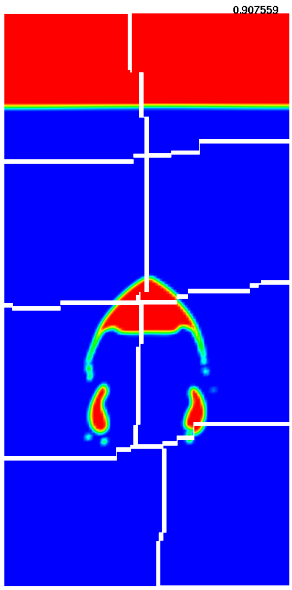


Figure 2. A splitting bubble moving across processing elements. The bubble algorithm tracks the number of splitting and merging bubbles and the history of their volumes between time steps across multiple processing elements.

Identification and tracking the history of distinct bubbles. The bubble-find algorithm distinguishes bubbles by assigning them unique IDs. The assignment of bubble IDs uses a recursive algorithm to sweep through the computational mesh, checking the void volume fraction in each visited cell. Starting from an arbitrary cell, the void volume fraction is queried followed by visiting neighbors of the cell

querying their void volume fractions. This procedure is continued as long as nonzero volume fractions are found. The volume fractions of the cells visited are accumulated and comprise the bubble volume. This is a depth-first-search graph algorithm and is more efficient than having to visit each cell of the mesh. Combining this algorithm, which finds a single continuous bubble, with flagging the already-visited cells and attempting to visit all not-yet-visited cells, allows finding all bubbles. This bubble-find algorithm is recursive as the same operation (querying the void volume fraction in a single cell) is carried out by a function that calls itself for the surrounding cells. Besides accumulating the void volume fractions to compute the bubble volume, the algorithm also keeps track of the previous-time bubble volumes for each unique bubble using an associative container. This allows tracking the history of each individual bubble as bubbles merge and split.

Serial prototype algorithm. The serial bubble-find algorithm, described above, has been prototyped in a separate C++ code to allow testing of the depth-first-search graph algorithm, the splitting and merging of bubbles, and the tracking of the bubble volumes between time steps. This step was a useful first step of the development as the topological part of the algorithm could be understood and tested in a simple setting without the influence of physics.

Parallelization. The algorithm described above works on a single PE and served the basis for the final, parallelized algorithm. The first step of the parallel bubble-find algorithm is the serial bubble-find algorithm described above, executed by each PE, yielding partial bubble volumes.

The bubbles can be large enough to reside on more than a single PE at any time, see Figure 2. The final step of the parallel bubble-find gathers the partial bubble volumes, found by each PE. The algorithm must be general as it must work for arbitrary number of bubbles of arbitrary shape and size, splitting and merging, cut or uncut by PE boundaries.

The final, gather-step of the parallel bubble-find algorithm takes the number of unique bubbles found by each PE as well as their current-, and previous-time bubble volumes and distributes them to all PEs involved. In other words, if a bubble resides on more than one PE, all PEs that contain parts of the bubble must see the same total bubble volume. This ensures that each PE will use the same bubble pressure to compute the influence of the bubble on its surrounding fluid. The gather-step consists of the following steps:

1. Generate global-to-all-PEs unique bubble IDs,
2. Generate a distributed graph of bubble parts connectivity for each bubble cut by a PE,
3. Compute the total volume of each globally-connected bubble and associate that volume with each of the parts comprising it,
4. Scatter-gather the computed total bubble volumes at previous and current time until the total bubble volume has reached all PEs the bubble resides on.

The gather-step of the bubble-find algorithm is designed to only use point-to-point communication for parallel efficiency. The output of the final, gather-step of the parallel bubble-find algorithm is two bubble volume arrays, containing the previous-, and current-time bubble volumes on all PEs corresponding to the (potentially multiple) bubbles on each PE. Based on these two volume arrays each

PE modifies its numerical solution for the pressure of the fluid surrounding its bubbles by applying the adiabatic formula for each computational cell that resides in a bubble and taking the bubble-cells out of the solution for the linear system computing the fluid pressure. This essentially provides a pressure boundary condition along bubble boundaries given by a dynamically computed bubble pressure.

A verification case

To verify that the correct solution is computed using the bubble model, a simple test case was set up with a known analytical solution.

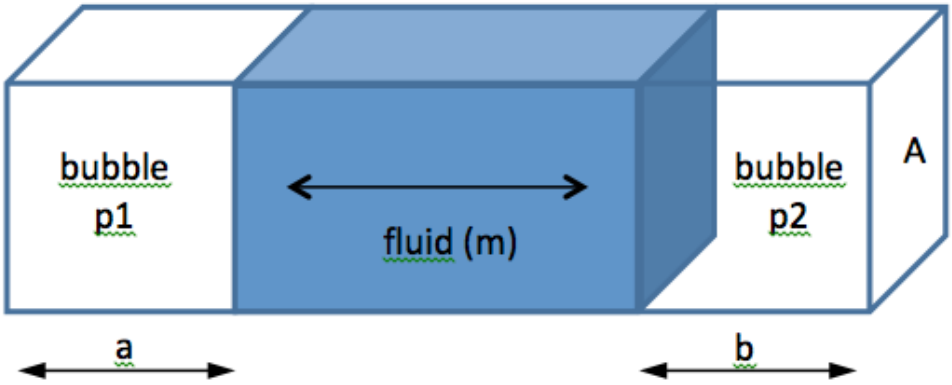


Figure 2. Horizontal channel with two bubbles surrounding a fluid in the middle of the channel.

Figure 3. depicts a horizontal channel with two bubbles surrounding a fluid in the middle of the channel. The materials at the ends are designated as bubbles by assigning zero densities, which Truchas identifies as void. This enables the bubble model algorithm. If the density is non-zero, the pressures are computed as usual – in every computational cell.

Initially, both materials are in a quiescent state and the initial bubble pressures are chosen to be unequal, $p_1 = 1.0$ and $p_2 = 1.1$. Since friction is neglected, the solution of this problem, assuming small amplitudes, is an oscillating fluid between the bubbles whose volumes and pressures follow sine waves. The equation governing the fluid displacement, x, of the small-amplitude motion is

$$m\ddot{x} + \omega^2 x = 0,$$

Where m is the fluid mass, and the oscillation frequency is

$$\omega^2 = \gamma p_0 A \left(\frac{1}{a} + \frac{1}{b}\right),$$

with $p_0 = (p_1 + p_2)/2$, and a and b are the length of the bubbles in the direction of motion (initially equal), see illustration above. Figure 4. shows the time-evolution of the computed bubble volumes. The analytical solution for the oscillation period is $T = 2\pi/\omega = 10.061$, and the maximum volume, $V_{max} = 1.605$, both well reproduced by the simulation.

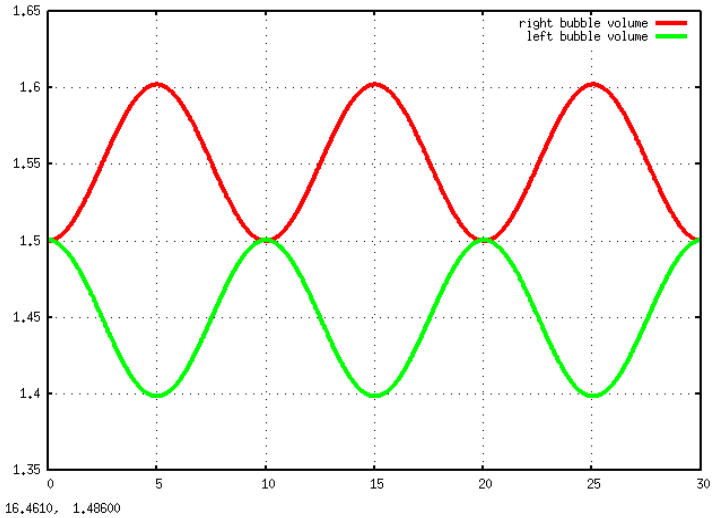


Figure 4. Time evolution of the bubble volumes in the oscillating fluid verification test case.

A validation case

A more complex test case is a single light bubble in a heavy surrounding fluid, depicted in Figure 5. The setup also includes a second bubble at the top, approximating a free atmosphere, whose pressure nevertheless changes in this test case, modeling a sealed container. The density ratio between the bubbles and the fluid is 1/100.

The case was run with and without the bubble model. The run without the bubble model exercises the existing fluid flow algorithm in Truchas and computes the flow field in both materials as usual, treating them as incompressible regions with different densities. The run with the bubble model does not solve the fluid equations inside the bubbles and treats the bubbles as compressible, while the surrounding fluid as incompressible materials. The initial bubble pressure of the rising bubble is assigned to be equal to the hydrostatic pressure at the center of the bubble.

Figure 5 depicts the initial condition, and the bubble volume fraction without and with the bubble model. As expected the two models behave qualitatively similar, i.e., the bubble rises as its density is lower than its surroundings, but the two models compute different solutions for the bubble topology and its rising speed. As the bubble model treats the bubbles as compressible materials, the rising bubble expands slightly, while the top bubble, approximating the atmosphere, is slightly compressed.

Summary

An alternative modeling approach for multiphase flow has been implemented. The new method is intended for large multi-phase flow calculations, where a phase (i.e., material) can be designated as void (e.g., gas bubbles), whose detailed velocity and pressure are of no interest, only its effect on the surrounding fluid flow. The method uses an adiabatic relation between the bubble volumes and pressures to compute the effect of bubbles on the surrounding flow and only solves the flow equations

in the fluid (and not inside the bubbles). Compared to the existing fluid flow algorithm, the new bubble model treats bubbles as compressible.

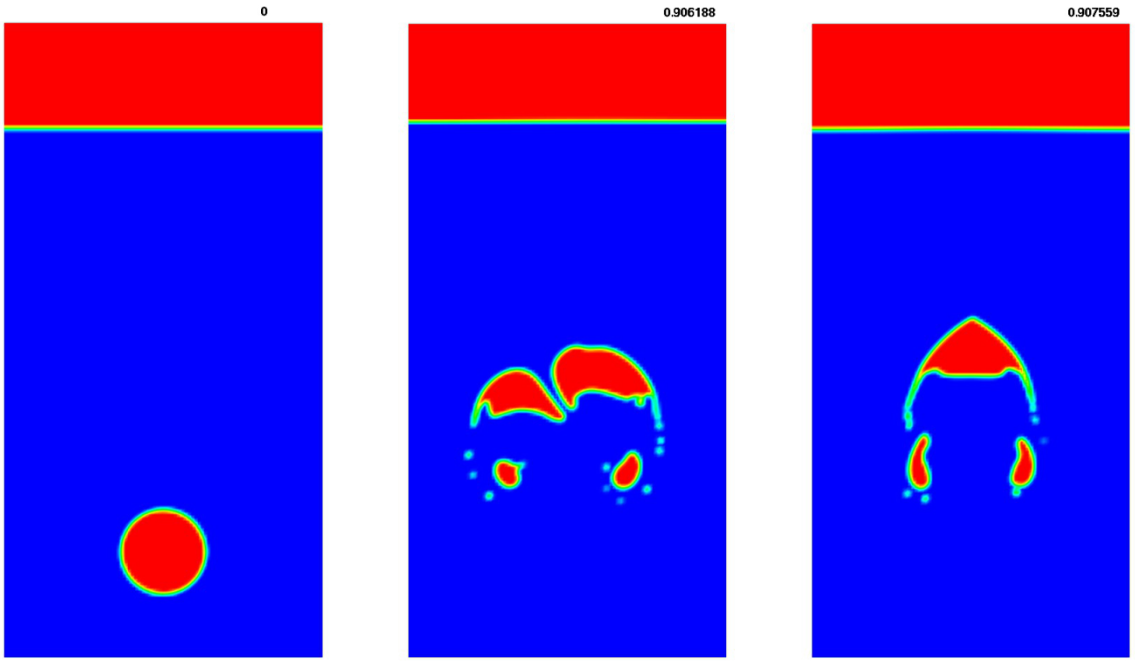


Figure 5: Light bubble rising and splitting with and without the bubble model – void volume fraction. Left -- initial condition; middle -- t=0.9, no bubble model; right -- t=0.9, bubble model.

Future work

While the algorithm is demonstrated to work for simple test cases, and in parallel, much more testing and validation are required to ensure robustness and production quality. The current implementation is a prototype and additional work is required to finalize the model and make it part of a future Truchas release.

Convolution versus finite element projection evaluation of surface tension

by

Rakesh Ranjan

Summary

Surface tension effects occur at an interface of two fluids when modeling multiphase flow. The earlier generalization of surface tension considered this effect acting as a tensile force on an interface. With the introduction of the continuum surface force (CSF) formulation of Brackbill et al. [1] this effect has been interpreted as a volumetric force acting over the interface thickness. This interpretation is done via the Gauss-Divergence theorem. Since the introduction of the CSF formulation of Brackbill this method has become a standard for implementing surface tension effects in different implementations [2-4].

The Los Alamos National Laboratory (LANL) code Truchas [5] has surface tension models which utilize convolution based algorithms based on Rudman kernels [6] and Willams kernels. The convolution algorithm requires a localized computation of the component volume fractions in the nearby cells to the interface. Such computations can be prohibitively expensive in parallel and engender load-balancing issues where one processor is computing the convolution integral and others await the results from such evaluations. This problem arises further due to poor scalability of the convolution algorithm used currently.

The task for this project was to implement a new surface tension model that is scalable and that also incorporates contact angle physics. Scalability required replacing the convolution procedure, and the initial approach was to replace the entire curvature calculation with a finite element (FE) based approach. It was discovered, however, that the smoothing produced by the convolution procedure is essential to obtain the correct estimates to the surface tension force and a simple implementation of the finite element gradient evaluation will not suffice for the purpose of evaluating the correct surface tension force. Two complementary approaches were taken subsequently. The first replaced the gradient and curvature evaluations with the FE based approach but using the existing convolution smoothing using the Rudman kernel. The second step replaced just the convolution procedure (which was the source of scalability problems) with an L2 projected-L2 smeared approach, and retaining the existing computation of the curvature. This work has unfortunately consumed the full year, and no progress was made on incorporating contact angle physics into the new surface tension model.

The first approach was to devise algorithms that perform better than the Rudman kernel convolution process that is in use currently. It was perceived thus evaluating gradients and curvatures in a finite element sense will provide better estimates to the curvature and surface tension force than the current finite volume interpretations for unstructured meshes. In this regard a new finite element based curvature calculation [7] was devised and incorporated in Truchas. It was further expected that such curvature evaluations may be more accurate compared to finite volume calculations. This was the first

work performed and resulted in the incorporation of a new option in the input file namely 'fe_curvature' which does this evaluation in a finite element sense.

The second approach was the incorporation of a new L2-L2 projection-smearing of the discontinuous VOF field to the discrete trilinear finite element space [8-10]. This projection has been found to provide smearing of the discontinuous VOF field and has been incorporated as the second method of modeling surface tension effects. Both methods performed well on sample problems solved and results are presented with the algorithms used in their development. This second approach is convolution free and does not require any ad-hoc estimates to the interface smoothing length. A new constant epsilon was devised which controls the amount of smoothing in the projected algorithm. The development process has been confined to the first bullet for the most part this year. Because of the limitations that were figured out with the smearing process and development of the finite element based procedures we have been confined to the first task. The next task is the incorporation of contact angle physics in Truchas. This remains to be implemented.

Introduction

The analysis support function is established within the Advanced Fuels Campaign (AFC) of the Fuel Cycle Research and Development (FCRD) program at the DOE Nuclear Energy Department to develop all necessary analysis tool sets to complete the performance and fabrication analysis of AFC irradiated metal, oxide and innovative fuels (including fuels and clads). This function targets three key activities: fuel performance sensitivity analysis, fuel fabrication, and performance analysis of fuels and reactors. We will develop, implement, and use fuel performance tools to assess AFC experiments. With the use of fully validated analysis tool sets, we will be able to optimize the advanced fuel design prior to irradiation and reduce the number of integral tests, saving time and investment. The assessment of fully validated tool sets with predictive modeling capabilities will help to better understand driving mechanisms of key phenomenon during the irradiation of AFC fuels and enable us to determine the right set of separate effects test (SET) validation experiments and the modeling requirements in order to develop fully predictive models. These models will allow us to interpolate in the fuel design space with higher confidence and less uncertainty, and also to extrapolate within untested regimes with determined uncertainties, resulting in increased confidence in safety calculations.

Two-phase flow problems, for example a liquid and a gas, separated by a moving, deforming interface are of interest in many research fields ranging from environmental sciences to nuclear industries [11-12]. The particular application we seek to address involves simulation of the casting of nuclear fuel rods. In this context it would be important to note that convolution-based procedures which are currently in use in Truchas do not provide sufficient flexibility of parallelism and thus are not sufficient for the actual casting simulation. A convolution free L2 projected L2 smeared algorithm was developed to address these limitations. In two-phase flow applications it is important to be able to describe the evolving

interface in space-time. For the tracking of the evolving interface in time different procedures have been developed. These can be broadly classified into two different approaches [12].

The first involves an explicit tracking of the interface. In this method the underlying mesh deforms with the fluid in motion. There is explicit motion of the nodal locations comprising the mesh with the moving fluid. While movement of the interface nodes is prescribed by virtue of the velocity field the adjustment of the inner nodes is arbitrary. Often the inner nodes are modeled moving as an elastic solid with a prescribed interface motion (elastic update method). Interface update methods are known to provide great accuracy, however their applicability remains limited in the case of severe interface motion. These are broadly classified as 'interface tracking' methods.

The second approach considers interface-capturing methods. The methods in this category utilize an artificial scalar to consider an implicit description of the interface. Amongst the methods are the volume of fluid (VOF), level set (LSET) and phase field methods. Volume of fluid adds an advection equation of this scalar advected with the incompressible Navier-Stokes equations. There is no body force in the VOF equation. As opposed to the VOF equation the LSET equation has curvature dependent forcing function terms. Because of these curvature terms it has often been mentioned in literature that VOF provides better mass conservation compared to LSET. On the other hand the presence of the curvature terms in the LSET methods endows it with the ability to handle complex topological changes in the interface geometry. The phase field on the other hand provides an energy conservative framework for tracking the motion of the interface. In this method the Helmholtz free energy of the system is conserved while the interface motion is described in space-time.

Background

Los Alamos National Laboratory (LANL) code Truchas [5] considers free surface flow with the volume of fluid (VOF) method. The code has been developed considering a cell-centered finite volume approach, which uses the VOF equation to track the dynamics of the interface. The VOF equation is advected explicitly in three dimensions. For modeling the interface dynamics the VOF equation is used which has a discontinuous interface. This means that across the different cells near an interface only the cell with a partial fill has a non-zero value of the VOF and the other cells change abruptly from zero to one. There is no smearing involved with this discontinuous piece wise linear interface construction (PLIC) interpretation.

Surface tension, which is an interface effect, was handled earlier as a surface force acting along the interface width. Brackbill [1] interpreted the surface tension force as a volumetric effect acting over the interface thickness. The thickness of the interface is usually taken to be around three to four (3-4) cell widths. This parameter has been defined as the interface smoothing length in the code. All the cells that reside inside the distance spanned by the interface smoothing length have the convolution integral smearing the interface onto their cell centers. This means that the cells which lie within the distance d from the interface have the convolution operation providing them a non-zero VOF value scaled appropriately by the distance from the interface.

Convolution based algorithms

The code has two different algorithms which utilize convolution based procedures for incorporating surface tension effects. The first considers the William's kernel for convolution of the VOF field, and the second considers the Rudman kernel. William's kernel being eighth order provides a very sharp interface and consequently does not provide good estimates to the curvature. Rudman kernel on the other hand utilizes a sixth order kernel and has been used earlier for solving surface tension problems. This kernel has provided reasonable solutions to sample problems with surface tension effects in earlier experiments with the code [13]. The Truchas code utilizes a projection algorithm for solving the incompressible Navier-Stokes equations [14-15].

The Rudman kernel which has been used to evaluate the surface tension force utilizes the sixth order Kernel. In order to have a smoother transition from the value of 0 to 1 the Rudman kernel is usually utilized during the convolution process. The convolution process can be considered as an integral over the distance function of

$$\tilde{C} = K * C(x) = \int_{\Omega} C(x')K(x' - x)dx'$$

Following such convolution procedures the gradient and the curvatures follow from the above formulae

$$\boldsymbol{n} = \frac{\nabla \tilde{C}}{|\nabla \tilde{C}|} \quad \text{and} \quad \boldsymbol{\kappa} = -\nabla . \boldsymbol{n}$$

For a function to be admissible as a kernel for use in the convolution process it must satisfy certain properties namely:

a. It must have compact support.
b. Must be monotonically decreasing with respect to r=|x|
c. Must be radially symmetric
d. Be sufficiently smooth, i.e. for some k≥ 3, K should be continuously differentiable
e. Have the normality property, i.e. integral of K over the domain of definition equals 1.
f. It should approach the smoothed Heaviside function in the limit interface thickness reduces to zero.

The constants in the Williams and Rudman kernels have been constructed to satisfy these properties. Scalability of the convolution process has been an issue since the convolution process is inherently difficult to parallelize. On unstructured meshes the convolution process does not perform well due to lack of symmetry of the distancing from the interface.

Due to these limitations it was found necessary to replace the convolution process with an L2 projected and L2 smeared algorithm [10]. The first task undertaken was replacement of the gradient evaluation used currently to those obtained from a finite element implementation with the convolved Rudman Kernel (in place) to make the gradient and curvature evaluations flexible for unstructured meshes. This has been accomplished and is mentioned in the first bullet (below). The reason for undertaking this

task was to be able to handle complex geometry and unstructured meshes. Finite element evaluation is the most appropriate for such cases because it can handle complex geometries. The second task was the development of a convolution free smearing and projection (L2-L2) procedure. This was required because of the scalability limitations mentioned above with a convolution based approach. This has been accomplished and has been included in the second section of this document.

Finite element curvature evaluation (fe_curvature)

The convolution process smears the discontinuous VOF field to adjacent cells within the distance of d from the interface, where d is the interface smoothing length. The interface smoothing length is taken approximately equal to three to four cell widths. The curvature evaluations with the Rudman kernel follow a finite volume approach which does not perform well on unstructured meshes. To remove such limitations on restrictions to structured meshes only we incorporated a new finite element approach for curvature evaluations. This new option incorporated in Truchas named 'fe_curvature' evaluates the curvature with a finite element interpolation of the VOF field. We tested this new curvature evaluation on two sample problems the static bubble and oscillating bubble problems.

1. **Static Bubble**

To validate the new curvature estimations over time, we consider the test case of a static drop in equilibrium without gravity. The exact jump in pressure across the drop is given by

$$\Delta P = \sigma\kappa$$

and the analytical expression for the curvature is given by

$$\kappa_{exact} = \begin{cases} \frac{1}{R} & in\ 2D \\ \frac{2}{R} & in\ 3D \end{cases}$$

The computational domain considered is a cube having side length of eight units. The drop is positioned at the center of the domain with a radius R=2.0. The surface tension coefficient σ was taken to be 73. The density inside the drop was taken as 1.0 and the density outside was taken as 0.10. This provided a density ratio of 10.0. The exact pressure difference is 36.5 in two dimensions (2D) and 73 in three dimensions (3D). Initially the velocity and pressure field are assumed to be zero. The CFL limit in all computations was taken as 0.4. Velocity boundary conditions are free-slip, i.e. the normal component of the velocity is zero. The computational domain was considered equi-spaced with equal spacing in the x and y directions. The capillary time step constraint taken as

$$\Delta t = \left(\frac{\bar{\rho}\Delta x^3}{2\pi\sigma}\right)^{\frac{1}{2}}$$

with $\hat{\rho}$ the average density between the two phases.

The reason for the generation of the spurious velocities is seeking the solution of the Navier-Stokes equations at the interface with varying densities. Another reason is the inaccuracies in the curvature evaluations. The inaccuracies in the curvature evaluation affects the surface tension force which enters the calculations as a body force in the momentum equations and causes generation of spurious currents.

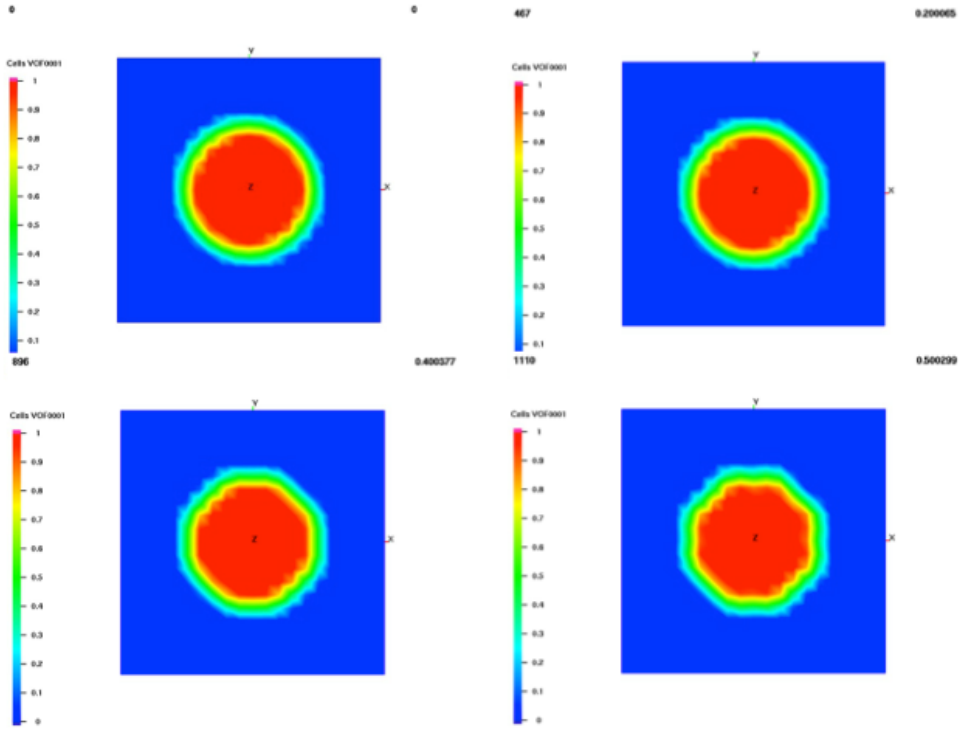


Figure 1. Deformed bubble shapes evaluated with Rudman Kernel.

Aware of the exact solution to the problem we compare the generation of the spurious velocities manifested in the form of deformed drop shapes at different steps of the transients for both the Rudman kernel approach and the finite element evaluation of the curvature. Figure 1 presents the deformed bubble shapes at times of 0, 0.2, 0.4 and 0.5 units for curvatures evaluated with the Rudman Kernel (left to right, top to bottom). There is considerable deformation in the bubble shapes at the end of the transient process (t-0.50).

Figure 2 provides the deformed shapes of the bubbles at the same time steps as provided with the finite element approach to evaluating the curvature. In the second FE based approach we utilized the Rudman kernel for the convolution process and augmented it with an FE based curvature estimation. When comparing we notice the finite element curvature estimations are more accurate since the final deformed shapes are less pronounced as compared to the convolution followed by a finite volume based curvature estimation. Thus the validation of the algorithm on the static bubble problem was achieved. With this problem solved we consider next the oscillating drop problem. This problem has often been considered as a standard benchmark problem for solving problems with surface tension effects.

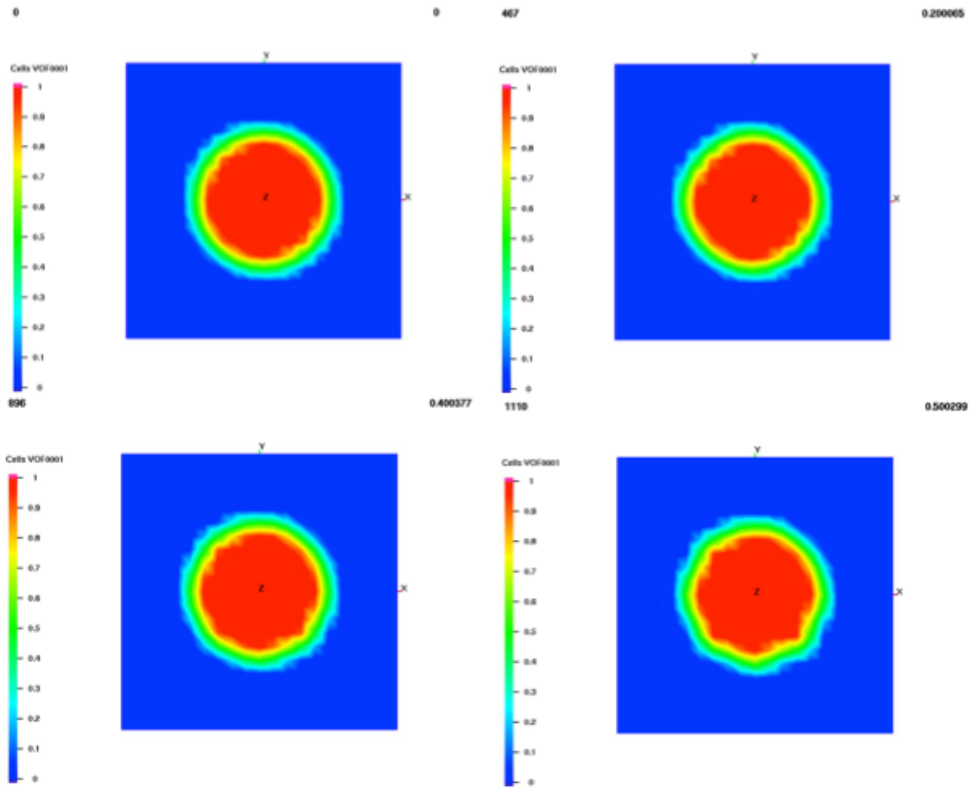


Figure 2. Deformed bubble shapes evaluated with Finite Element Curvatures.

2. Oscillating Drop

Oscillating drops represent a standard test case for surface tension models. We consider the problem studied in [2]. Initially, the drop interface is an ellipse given by $x^2/9+y^2/4=1$. The drop is placed in a computational domain of size 20x20, partitioned with a 64x64 mesh. Gravitational forces are absent. The fluid properties are, $\rho_1 = 1$, $\rho_2 = 0.01$, $\mu_1 = 0.01$, and $\mu_2 = 5.0x10^{-05}$ and the surface tension coefficient was taken as $\sigma = 1$.

Due to the surface tension force the droplet oscillates. We examine the deformed shapes of the drop at different time steps. Enough time is allowed for the droplet to oscillate and reach a periodic frequency of oscillation. From the oscillations of the bubble the time period of one oscillation was calculated as T= 11.0. From these calculations the frequency of oscillation is determined as 0.0909. The simulation was carried till an end time of t-24 to verify the stability of the oscillating bubble due to surface tension and the constant period of oscillation.

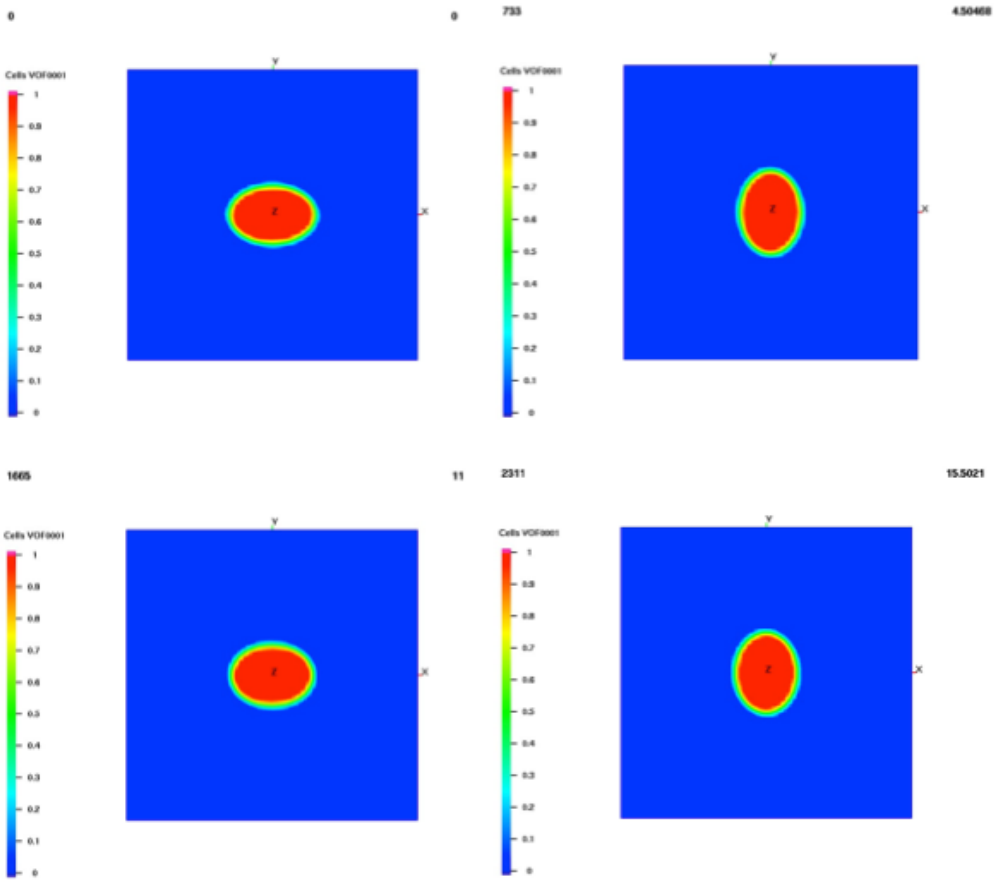


Figure 3. Oscillating bubble shapes at different times (of the transient).

Convolution free (L2 projected) algorithm

With the limitations of the convolution process in mind (scalability) we incorporate a new procedure namely L2 projection and L2 smoothing of the volume of fluid color function to effect smearing. This procedure has been mentioned in literature to provide smearing of the interface [10] by virtue of the existence of the diffusion term which serves to broaden the discontinuous interface. The smoothing operation or this smearing process is incorporated by adjusting the parameter epsilon mentioned in the equation below.

Let us denote the smoothed field we obtain from this procedure as $\tilde{\varphi}$ and the input discontinuous color function to the L2 projection as φ. The equation for the smoothing operation is provided by

$$\underbrace{min}_{\tilde{\varphi}} \int_{\Omega} |\tilde{\varphi} - \varphi|^2 \, d\Omega + \varepsilon \int_{\Omega} |\nabla \tilde{\varphi}|^2 \, d\Omega$$

The smoothing operation can be considered as a minimization of the distance between the discontinuous VOF field φ and its smooth approximation $\tilde{\varphi}$ whose derivatives are regular. The smoothing of volume fractions in volume of fluid algorithms for multiphase flows is known to introduce artificial errors near the boundaries of the physical domain (spurious currents). The approximation of the surface tension effects near the boundaries requires for instance the introduction of ghost cells

outside the domain. This drawback can be corrected by the above approach. Two different approaches were taken in this algorithm. The first approach integrates all the terms in the stiffness matrix with full integration quadrature. The second approach integrated a part of the stiffness matrix with reduced integration and part of the stiffness matrix with full integration. These methods were included as option 1 and option 2. Coding both the methods has been accomplished and both provide good results.

There are analytical solutions available for the projection problem (stated above) in one dimension. The three dimensional problem was reduced to one-dimension and solved to benchmark the new Truchas code. Benchmarking of the code was done separately in each orthogonal direction X,Y,Z (results not shown). To further test the implementation for unstructured meshes we orient the VOF field diagonally cutting across the square shaped domain. Epsilon values were varied to verify the effect of smearing on the original discontinuous VOF field. Figure 4 presents the input VOF and the smeared field at the end of the projection step for epsilon values of 0, 0.005, and 0.02 respectively. The figures have been annotated appropriately with different epsilon values. Amongst the advantages of the above procedure are it does not depend on the distancing operation necessary for convolution based algorithms. Further there is no limitation on the generation of acceptable results only for structured meshes.

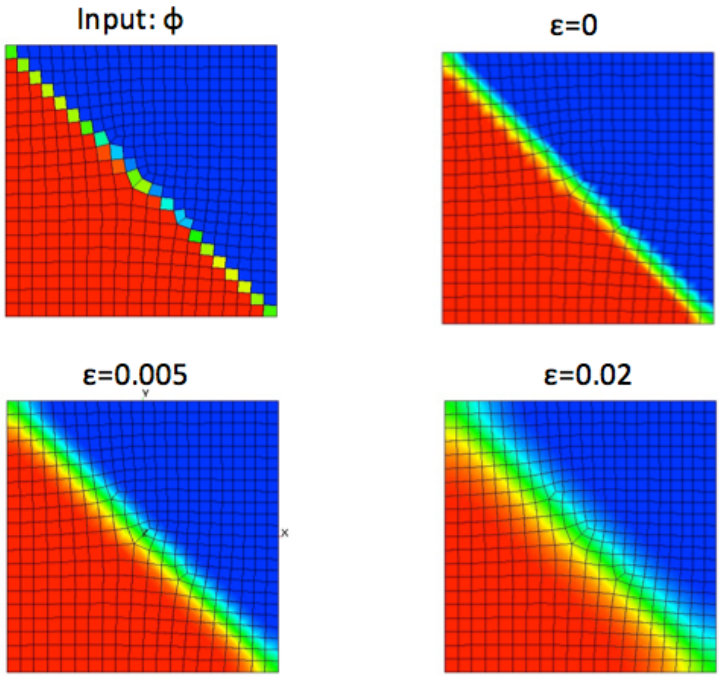


Figure 4. Input VOF field and output for different epsilon values.

Figure 4 presents an example where smearing has been achieved effectively for an input of a diagonally oriented VOF field on an unstructured mesh. Both the opposite diagonals were checked for smearing for verification purposes. However results have been presented only for the top left diagonal.

With the above example we demonstrate effective smearing on unstructured meshes. The Figure 4 above thus clarifies we replaced the earlier convolution algorithm with a L2 projected L2 smeared approach. Both convolution and L2-L2 apporach provide smearing of the original discontinuous VOF

field. We show in the figure that the earlier convolution operation that was replaced with L2-L2 approach provides the necessary smearing needed for subsequent gradient and curvature estimations. We further tested this new algorithm for different test problems. We are presenting three different problems for verification purposes. The problems were the static bubble, advection of a bubble in a channel and deforming bubble at different Bond numbers. These problems have been determined to be standard when studying surface tension effects.

a. Static bubble

This problem has been defined earlier. As mentioned previously the domain considered was taken as [-4.0,4.0]x[-4.0,4.0]x[0,1.0] with a unit width in the Z direction. A bubble of radius 2.0 units lies at the origin.

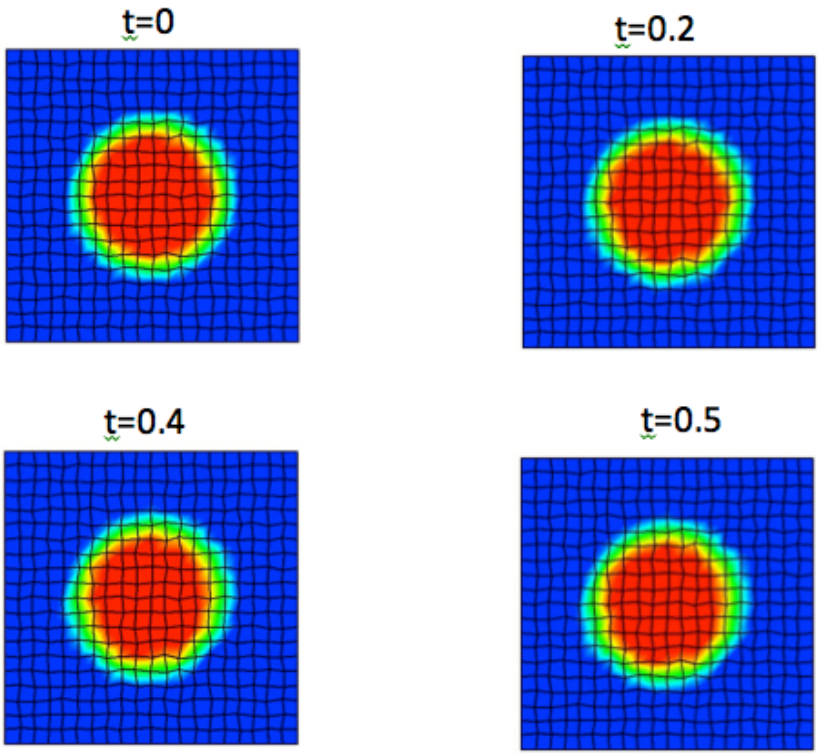


Figure 5. Static bubble solved on an unstructured mesh.

The domain was meshed with an unstructured mesh. The unstructured mesh was created with a random perturbation of the coordinates by 12.5% with a random scheme. The simulation was performed with an end time of 0.5 and time step size of $1e^{-04}$. The constant coloreps (smoothing parameter) was named as the value of epsilon in the code. This constant was taken as 0.005 for the simulation. As can be seen from the figures, the problem when solved on an unstructured mesh creates spurious currents but they remain bounded because there is no excessive motion or deformation of the bubble shapes over time.

b. Bubble advection with surface tension

Let us consider the advection of a bubble within a second fluid with surface tension effects. The domain was considered as [-2.0,2.0]x [-3.0,7.0]x [-0.05,+0.05]. The mesh was constructed with spacing of 0.20 along the X and Y directions providing a discretization of 20x50. A randomly perturbed mesh was specified with a perturbation of the node coordinates by 10%. The spacing in the Z direction was set at 0.10 providing a cell width along Z.

Initially the fluids were specified to be in a state of quiescence. The cylinder was specified to have a radius of 1.25 units. For the advection problem all the faces were assumed to have free-stream velocity with the Y-component of velocity specified as 1.0 unit. The transient was simulated till t-4.0 time units. The initial time step was specified as 0.001 which is lesser than the surften number restriction for the problem of 0.005. The surface tension coefficient was taken as σ=0.73 at the interface. The smearing constant epsilon (coloreps) was taken as 0.50.

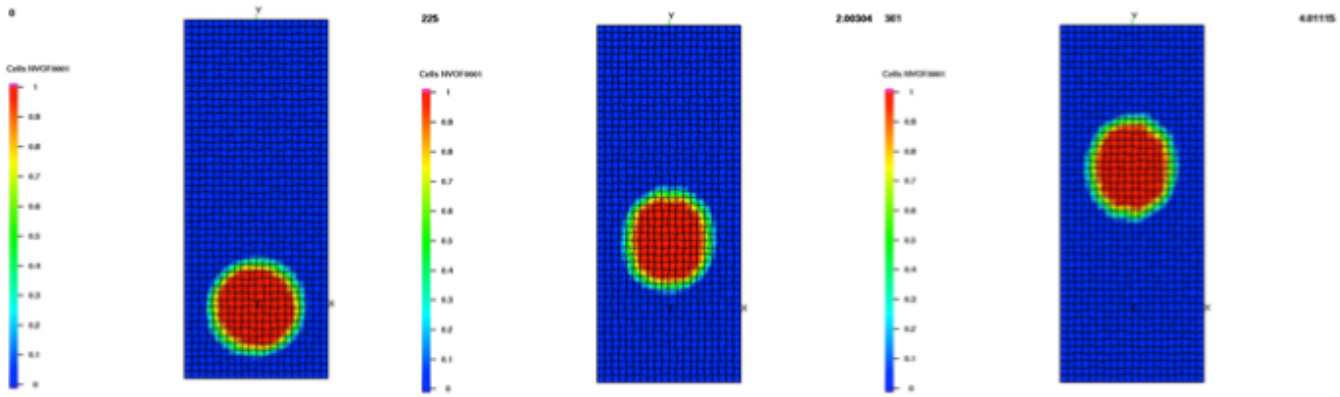


Figure 6. Advection of a bubble in a long channel.

Figure 6 presents the advection of a bubble at time steps of t=0.0, 1.5 and 4.0 units. The bubble deforms slightly while undergoing advection inside the thin channel. This example further validated the smoothing operation and correct evaluation of the surface tension force for an unstructured mesh. It is to be noted that the original surface tension model exhibited more pronounced deformations as compared to the L2-L2 formulation. The present approach performs better than the Rudman kernel convolved procedure for this problem for both structured and unstructured meshes. The superiority of the present formulation and flexibility of the approach is further demonstrated thus.

c. Rising of air bubble in water

We consider next the rise of air bubble in water by buoyancy forces. The characteristic non-dimensional number for this situation is the Bond number, or the ratio of the gravitational forces to surface tension forces.

$$Bo = \frac{\rho g D^2}{\sigma}$$

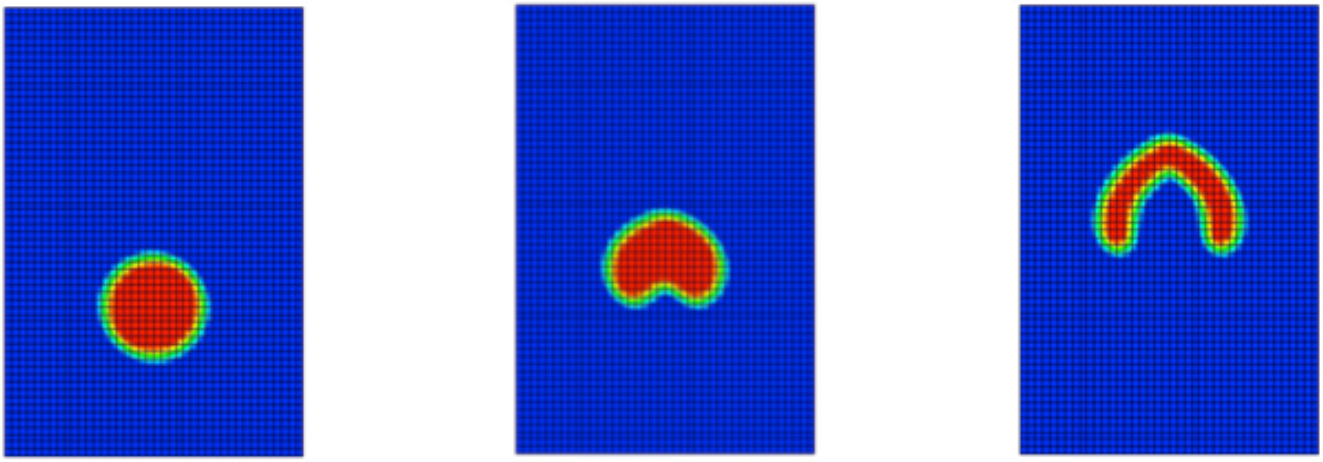


Figure 7.Computed shapes at times t=0, 0.20 and 0.50 with Bond numbers Bo_1=73.4 and Bo_2=59.83x10^3.

where, D is the bubble diameter. The governing equations are the Navier-Stokes equations on the computational domain [-1,1]x[-1,2]. A drop of radius R=1/3 is initially placed at [0,0]. The mesh is 40x60. For the first test case, the fluid properties of air (fluid 1) and water (fluid 2) are: ρ_1=1.226, ρ_2=1000, μ_1 = 1.137 and μ_2 = 1.137x10^{-05} and the surface tension coefficient σ=0.0728. The downward acting acceleration due to gravity was taken as 9.8. Figure 7 presents the deformed shapes of the initially circular bubble when undergoing deformations with Bo_1=73.4 and Bo_2=59.83x10^3 with surface tension σ=0.0728. For this case observable differences in the bubble shapes is not evident between the convolution based and projected algorithms for solving this problem. This is because in this case the surface tension force is not dominant i.e. the flow is primarily driven by buoyancy forces.

For the second case the only parameter changed is the surface tension coefficient which is increased to σ=728 corresponding to smaller Bond numbers of Bo_1=7.34x10^{-03} and Bo_2=5.983. For this simulation we observe less deformation in the bubble shapes for different curvature and surface tension models.

Figure 8 presents the computed shapes at times of 0, 0.35 and 0.50 for the second case. For this case there are differences observed in the computed shapes with differences in the methods of evaluating curvatures and surface tension forces. For our case with the L2 projection algorithm we observe bubble pinch-off at non-dimensional times of t-0.50.

Conclusion

Two different approaches for incorporating surface tension effects in the code Truchas were implemented and validated for benchmark problems. These approaches considered both a convolution followed by a finite element based curvature evaluation for an interface, and a secondly a convolution free (L2 projection) approach. The convolution augmented with a FE curvature algorithm was utilized to solve the static bubble and oscillating bubble problems and results were presented. The convolution free algorithm had two options one of full integration and reduced integration of the mass matrix terms. The convolution free (projected) algorithm was used to solve the static bubble, bubble advection, and the rising of an air bubble in water at different Bond numbers. The results presented show the robustness of the convolution free algorithm for solving problems on both structured and unstructured meshes. With the convolution based algorithm followed by the finite element approximation of the gradient we obtain superior results on the static bubble problem as compared to Rudman kernel evaluations.

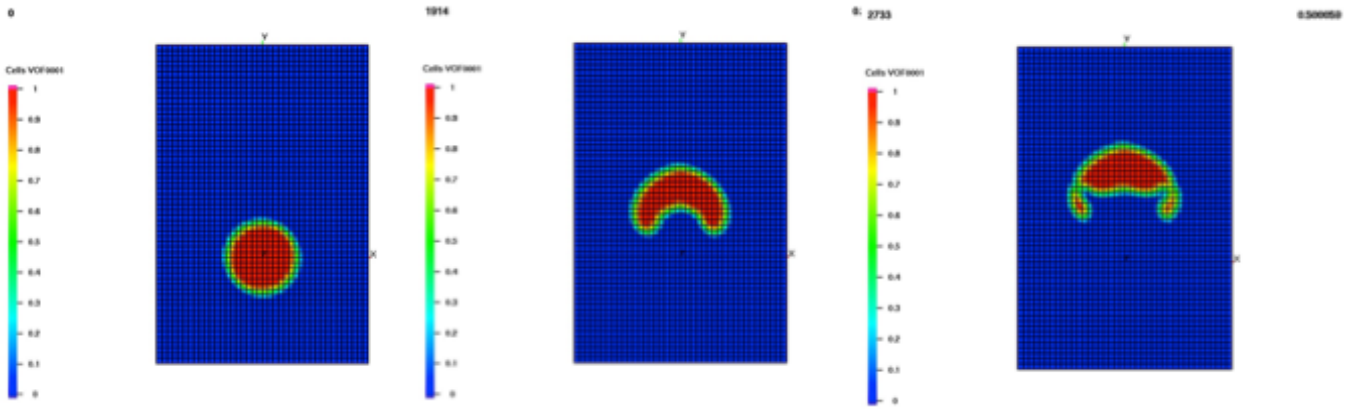


Figure 8. Computed shapes at times t=0, 0.35 and 0.50 with Bond numbers Bo_1=7.34 x10^{-03} and Bo_2=5.983.

References

1. J.U. Brackbill, D.B. Kothe, C. Zemach. A continuum method for modeling surface tension. Journal of Computational Physics. 100 (1992), 335-354.
2. D.B. Kothe, W.J. Rider, S.J. Masso, J.S. Brock. Volume tracking of interfaces having surface tension in two and three dimensions. American Institute of Aeronautics and Astronautics. (1996), 1-24.
3. S.J. Cummins, M.M. Francois, D.B. Kothe. Estimating curvature from volume fractions. Computers and Structures. 83 (2005), 425-434.
4. D. Jamet, D. Torres, J.U. Brackbill. On the theory and computation of surface tension: The elimination of parasitic currents through energy conservation in the second-gradient method. 182 (2002), 262-276.
5. The Telluride Team, Truchas: physics and algorithms, Technical Report LA-UR-03-0166. Los Alamos National Laboratory, 2003.
6. M. Rudman. Volume tracking methods for interfacial flow calculations. Int. J. Numer. Meth. Fluids. 24 (1998), 671-691.

7. S. Nagrath, K.E. Jansen, R.T. Lahey. Computation of incompressible bubble dynamics with a stabilized finite element level set method. Comp. Methods in Appl. Mech. Engg. 194 (2005), 4565-4587.
8. A. Caboussat. A Numerical method for the simulation of free surface flows with surface tension. Computers and Fluids. 35 (2006), 1205-1215.
9. A. Caboussat, R. Glowinsky, J.M. Sicilian. Computation of the normal vector to a free surface by a finite element-finite volume mixed method. C.R. Acad. Sci. Paris. 343 (2006), 431-436.
10. A. Caboussat. Numerical methods for non-smooth L1 optimization: applications to free surface flows and image processing. Inter. J. of Numerical Analysis and Modeling. 6 (2009), 355-374.
11. K.W. Lam. A numerical surface tension model for two-phase flow simulations. M.S. Thesis, Institute of Mathematics and Computing Science. (2009).
12. A.K. Tornberg. Interface tracking methods with application to multiphase flows. PhD. Thesis. Royal Institute of Technology (2000).
13. M.M. Francois, S.J. Cummins, E.D. Dendy, D.B. Kothe, J.M. Sicilian, M.W.Williams. A balanced-force algorithm for continuous and sharp interfacial surface tension models within a volume tracking framework. Journal of Computational Physics, 213 (2006), 141-173.
14. A.J. Chorin. Numerical solution of Navier-Stokes Equations. Math. Comput. 22 (1968), 745-762.
15. A.J. Chorin, J.E. Marsden. A mathematical introduction to fluid mechanics, Springer, New York, 1993.

Modeling and simulation of U-Zr casting experiments by Flow3D

by

Rakesh Ranjan

Abstract

Computational simulations of gravity casting for metallic U-Zr nuclear fuel rods were performed with the flow solver Flow3d. Numerical simulations were validated with experimental data obtained by Idaho National Laboratory (INL). The experimentally measured transient temperature profiles inside the casting apparatus were matched by adjusting primarily the heat transfer coefficients between melt and the mold at different locations. The volume of the rods cast, length of rods were predicted through the transient casting process and were found to be in reasonable agreement with experimental data. A sensitivity analysis with vent locations, pressure, mesh refinement, and effects of surface tension at the interface was performed. The validated modeling parameters will be used in the simulation of larger size caster with larger outputs in the coming fiscal year.

Introduction

To improve the manageability of spent nuclear fuels in storage repositories, metallic and oxide fuels are being designed that burn actinides such as Pu, Np, Am, and Cm, which cause heat load problems. Actinide burning in fast nuclear reactors has been the traditional approach [1]. Numerical simulations for the casting problem have been investigated in research efforts previously [2-6]. Renewed attention to this problem is important due to the casting of different types of nuclear fuel with constituents such as Pu, Zr, and U along with Am and Np.

In an earlier work, the simulation of the casting problem along with a parametric study of variation of different parameters affecting the casting process was performed with Flow3d [1]. In that paper however, the model presented utilized heuristic parameters while modeling the casting process. In the earlier paper an extensive parametric study was performed with a set of numbers as input (high, low, and median values) for the casting problem. However, there was no experimental data to validate the modeling parameters and casting model. Recently, INL conducted two U-Zr casting experiments. In this paper, we extend previous work and provide comparison with two different casting experiments. Different metrics are established to benchmark Flow3d calculations with experimental data such as length of rods cast, volume of rods, and transient temperature profiles at different locations along the cavities of the pins in the inner mold of the casting apparatus.

Model parameters, model tuning using INL casting experiments, and comparison of volume and masses

A Flow3d model of the caster was constructed using exported solid models of inner and outer mold, crucible, base plate, and casting charge. These were imported as STL files into Flow3d and the initial configuration of the charge was specified based on the experimental data of the initial weight of the melt (before it flows down the mold apparatus).

Two different configurations of the charge as a melt were specified (with different volumes of charge). This was done to compare simulation results with experimental data corresponding to 100 gm and 200 gm volumes of charge obtained from INL. The control volume (finite volume) mesh generated from Flow3d constructs the mesh on a Cartesian domain with 82x82x236 grid cells for an outer domain size varying from [-0.041,0.041]x[-0.041,0.041]x[-0.0045,0.17275]. This provides an equi-spaced mesh in the x, and y-directions. This is necessary for the correct curvature estimation in the surface tension evaluations within the continuum surface force (CSF) framework. From previous preliminary numerical experimental studies for this problem with different mesh sizes at Los Alamos National Laboratory (LANL) this mesh was reported to capture all the flow metrics of interest with sufficient accuracy [1]. The above mesh results in a total of 1586864 control volumes which are partitioned into blocks for parallel processing.

Parallel implementations of the Flow3d program were effected with a block distribution of the mesh into two to four mesh blocks. The entrapped gas Argon was assumed to behave as an ideal gas with a gas constant c_p/c_v of 1.667 and pressure of the void region was specified as the pressure of mold cavity of 85,726 Pa (85.7 kPa) for the initial simulations. The assumption in using the adiabatic model is that the inertia of the fluid is much higher compared to the inertia of gas. This is normally considered a very good approximation since the density of U-Pu-Zr alloy used is approximately 10,600 greater than Argon, thus the gas inertia of Argon is negligible. A very low value of the heat transfer coefficient was specified for the interface between the melt and the entrapped gas so as to minimize the heat loss to the bubble. Acceleration due to gravity for the gravity pour was specified as -9.81 (m/s^2), driving the flow downward.

The solidification profile used in the model assumes release of latent heat of fusion before the fluid changes phase from a liquid to solid. Table 1 in Crapps et al. [1] provides values of the thermal conductivity of the molten and solid states comprising of uranium 10% zirconium mix along with the liquidus and solidus temperatures. The latent heat of fusion is further provided for the phase change phenomenon.

Table 1. Temperature dependent variation of thermal conductivity and rho*cp.

	Thermal conductivity (W/mK)	Density*Specific Heat*10^6 (J/m^3K)
200	88.06	1.22
300	78.32	1.566
400	70.03	1.877

500	63.07	2.156
600	57.33	2.405
700	52.66	2.625
800	48.97	2.818
900	46.13	2.986
1000	44.01	3.131
1100	42.5	3.255
1200	41.48	3.358
1300	40.83	3.444
1400	40.43	3.514
1500	40.15	3.57
1600	39.89	3.613
1700	39.51	3.645
1800	38.9	3.668
1900	37.94	3.684
2000	36.51	3.695

Thermal conductivity determines the heat transferred from within the domain of the fluid region to the inner and outer molds. Specific heat and density determine the heat capacity of the melt and the inner and outer molds. There are various components of the mold assembly namely inner mold, outer mold, crucible, charge, stopper and the base plate. Heat transfer coefficients were specified between each of the components in the assembly. The heat transfer coefficients were empirically fit from the earlier paper by Crapps et al [1] and the INL test simulations. The heat transfer coefficients were required to be a constant value and are not required to be varied based on Flow3d input requirements. The specific values used in the simulations are tabulated in Table 2 for both the full charge and half charge models.

Table 2. Heat Transfer coefficients between different components.

Mold Assembly Component # 1	Mold Assembly Component # 2	Heat Transfer Coefficient (full charge) $W/(m^2 \bullet K)$	Heat Transfer Coefficient (half charge) $W/(m^2 \bullet K)$
Inner mold, outer mold, or Crucible	Melt	1100	1200
Inner mold	Crucible	40	0
Outer mold	Inner Mold	10	100
Inner mold	Base Plate	100	100
Outer mold	Crucible	40	100
Inner mold	Base plate	100	100

The inner and outer molds are made of Graphite2020 from Carbone of America. Thermal properties of Graphite were determined from literature and variation of the thermal conductivity and heat capacity were included in the Flow3d model as a function of temperature.

By adjusting heat transfer coefficients shown in Table 2 the experimentally measured temperature histories are matched as shown In Figures 1 & 2. Figure 1 presents the reasonable agreement between the measured thermocouple readings for the temperatures obtained at a height of 0.03921 m (bottom) from the bottom of the base plate with Flow3d simulations for the 100 gm run. Flow3d temperature predictions were obtained with the identification of a probe located at the specified height from the bottom of the baseplate. The maximum deviation between the simulation results and experiment was found to be 3 °C. Considering the absolute magnitude of temperatures which are in the range of 250 °C this disagreement can be considered small. Further this disagreement provides a modeling accuracy of 1.2% which is less than 2% engineering accuracy.

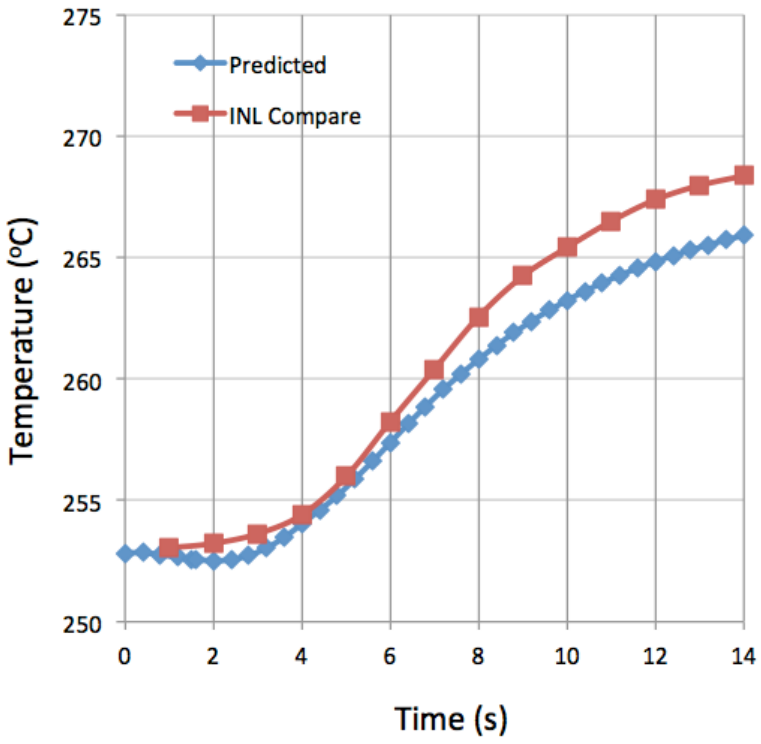


Figure 1. Predicted profile vs. experimental data for 100 gm simulation.

During the casting experiments temperature measurements were made at two separate locations along the length of inner mold. The locations of the thermocouple readings were specified as 0.03921 m (bottom) and 0.111 m (top) from the bottom of the base plate. Figure 2 shows the temperature histories at two locations with the adjusted heat transfer coefficients. The maximum deviation between the predictions was found to be within 2.6°C for the bottom temperature predictions and 5.1°C for the top thermocouple. The differences between predictions and data are reasonable. Both the deviations 0.81% and 1.2% respectively lie within the engineering accuracy of 2%. Further it was realized that the

top of the mold retains some residual charge which sticks to the surface of the inner mold which can account for the slightly higher temperature deviation for the top thermocouple measurements.

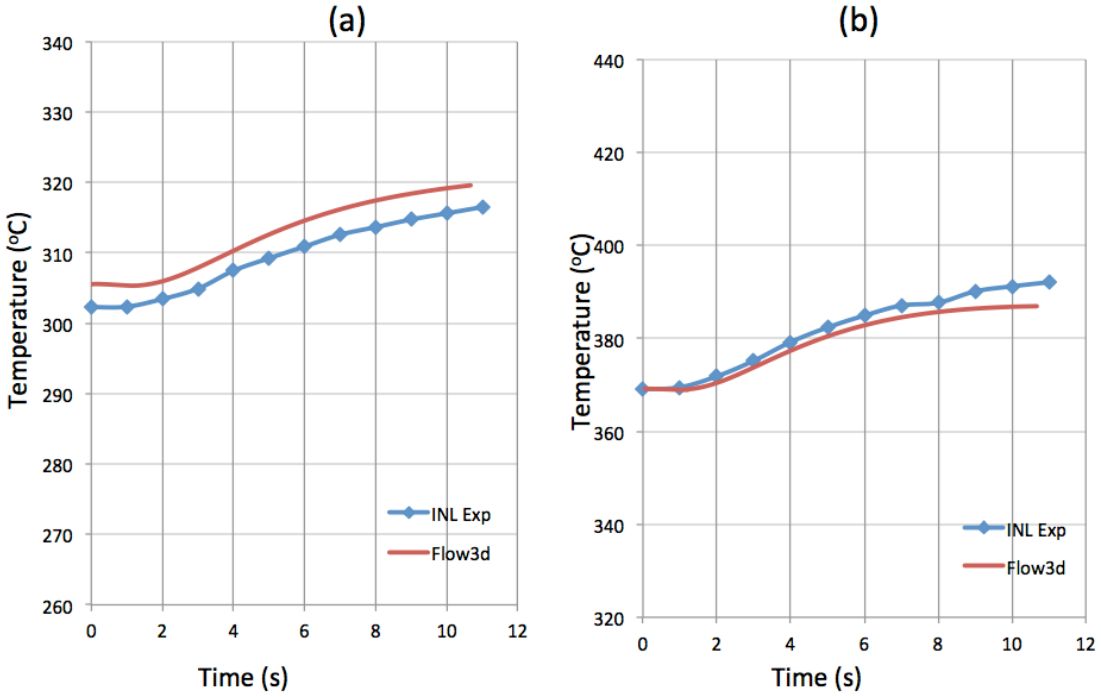


Figure. 2. Predicted temperature profile vs. simulation for 200 gm charge.

a. bottom of mold b. top thermocouple location

Using the heat transfer coefficients given in Table 2, the rest of experimentally measured quantities are compared.

Experimental data was provided by INL where experimental casting of the rods was determined for two different charges with either half or full charge. The first experiment utilized charge that was half the volume required to obtain full fill of the rods. This simulation is mentioned as the 100 gm run. The second experiment had twice the volume of charge specified that completely filled the rods and is mentioned as the 200 gm run. Experimental data provided temperature profiles at different sections along the length, in addition to composition of the final casted rods and the initial charge. The initial pressures in the casting apparatus were also provided in the experimental data. The weight of the rods as they were cast was recorded. Locations of the thermocouples where the temperature measurements were made and the locations of vents were identified from GACS drawings and the drawings of the mold cone. The vent locations were identified because the vents aid the release of entrapped Argon gas. All these parameters were utilized to set up the model and to obtain the volume of the rods cast, length of rods, and the transient temperature traces through transients as validation metrics for the simulation.

Additional experimental data included the pressure inside the chamber, weight of rods cast, and the volume of the three pins at the attainment of steady state. The first INL run required simulating the

casting process when half the charge was used in the casting simulation. For this case lengths of the rods reached half of the maximum rod lengths. The lengths of the rods from Flow3d were obtained after breaking up the domain into a hundred sampling points. At these sampling points at which the volume of the fluid field (VOF) was found to be greater than 0.50 was identified as the solidified melt and lesser than 0.5 was identified as void region (occupied by Argon gas). Table 3 provides the volume of the rods cast for the 100 gm run. There is a reasonable agreement between simulation results and experimental data. The simulation over-predicted Rod 3 volume. Due to the complex flow structure and the convective non-linearity while the rods are being cast there is asymmetry in the flow field in the simulation where the melt volume is specified as half of the total rod volume. Disagreements in the experimental results and simulation data could account for the non-uniformity of the incoming flow to the rods.

Table 3: Volume of rods cast for 100 gm charge (cm^3).

	INL Experiment	Flow 3d (simulation)	(DataSim)/Data Simulation
Rod 1	1.425	1.35	5%
Rod 2	1.33	1.15	14%
Rod 3	0.899	1.1875	-32%

The lengths of the rods cast for the simulation results presented in Table 3 have been provided in Table 4. Lengths of the rods are in reasonable agreement with experimental data. Due to the complex non-linear nature of the flow field falling down the casting apparatus and the differences in the advancing front as it hits the inner mold we obtain slightly different metrics on the 100 gm charge as compared with INL experiments. Figure 3 presents the lengths of the rods as they were pictured after the casting (middle three pins) for both the 100 gm and 200 gm runs. As can be seen there are breaks in the rods. A small amount of residual solidification resulted in the presence of two drip residues as shown on the left of the cast pins (Figure 3) for the 100 gm.

Table 4: Length of rods cast for 100 gm charge (in).

	INL Experiment	Flow 3d (simulation)	(Data-Sim)/Data Simulation
Rod 1	3.756	3.42	9%
Rod 2	3.516	3.09	12%
Rod 3	2.37	2.699	-14%



Figure. 3. Pictures of cast nuclear fuel rods for (a) 100 gm (b) 200 gm experiments.

Extensive testing was done on each piece of the cast rods to determine the metals distribution. The volume of the rod(s) was obtained from such analysis after utilizing a weighted average of the individual densities of the components found from above. The length of the rods from Flow3d was determined by identifying a hundred sampling points along the length in the casting apparatus and identifying the volume of fluid locations greater than 0.5 as the solidified melt. The transient casting process (Figure 4a) along with the final profile of the three rods colored with temperature contours along the length of the pins is presented in Figure 4 (b). Due to the usage of the bubble model which models gas entrapment inside the apparatus breakage of the rods is evident along the length. The 100 gm charge provided a smaller length of the rods compared to the 200 gm charge (Figure 3).

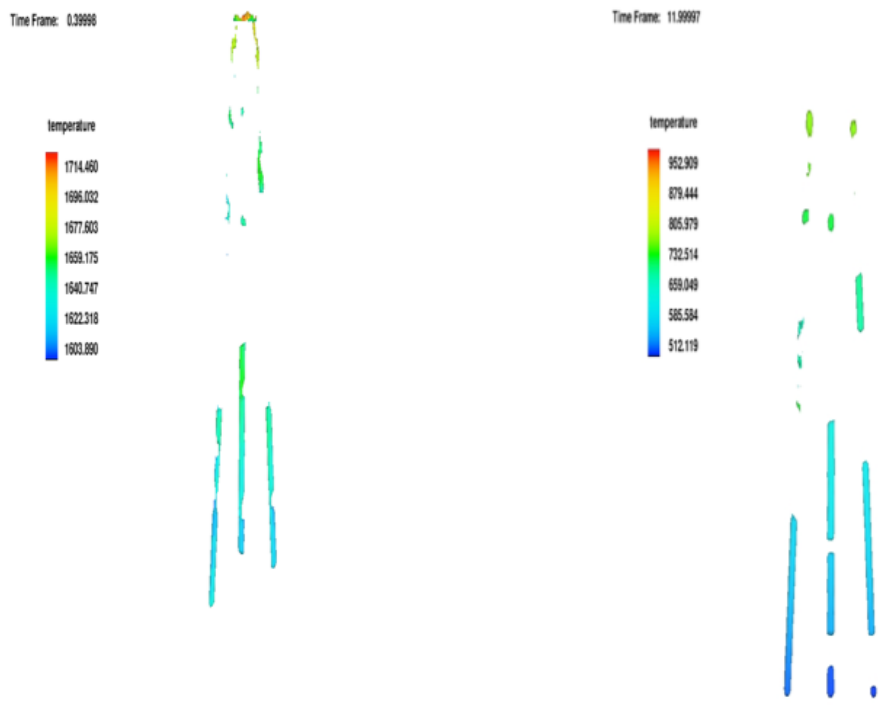


Figure. 4. Simulation for 100 gm run (a) Transient evolution of rods cast (b) Final cast profile.

Table 4 presents the volume of rods as the cavity inside the inner and outer mold is filled with the flowing melt for the 100 gm simulation. Figure 5 presents the transient filling process inside Rod 1 with time. For the 100 gm simulation we observe steady state for settling of the fluid is reached at 1.5 s of simulation time. Table 5 presents the volume of the rods cast for the 200 gm charge simulation. A larger value of the charge was used than the previous simulation to exercise the simulation capability of Flow3d for the casting of full rods. Assuming an equi-distributed volume of the charge we obtain an approximate volume of charge of 3.79 (cm^3) whereas Flow3d provided volumes of the rods cast varying from 3.5 (cm^3) through 3.8 (cm^3) respectively. Relative to test 1 the prediction error decreased.

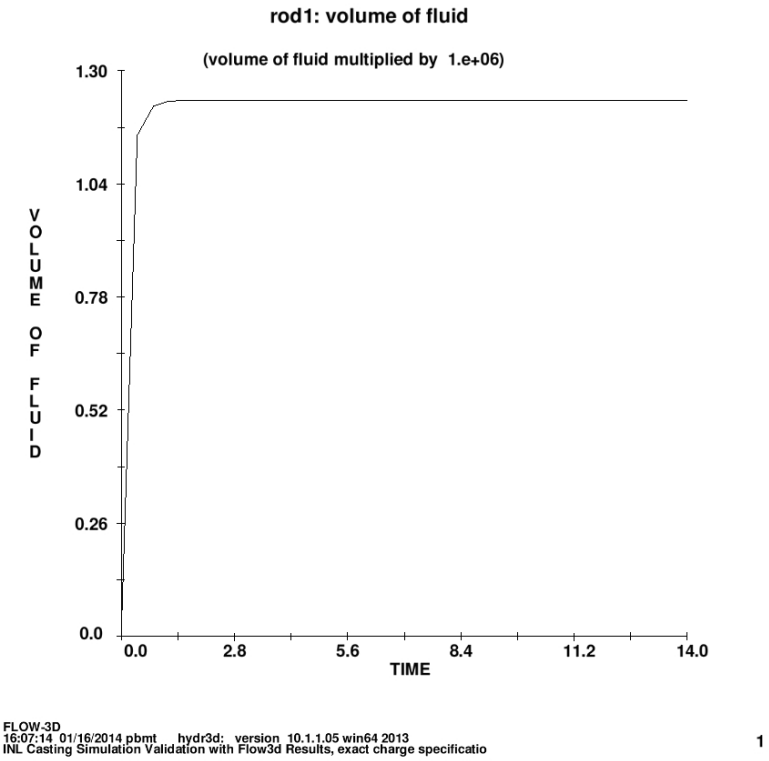


Figure 5. Predicted volume of rod1 (m^3) for 100 gm simulation.

Table 5: Volume of rods cast for 200 gm charge (cm^3).

	INL Experiment	Flow 3d results	(Data-Sim)/Data
Rod 1	3.79	3.68	3%
Rod 2	3.79	3.54	7%
Rod 3	3.79	3.39	11%

Experimental results and Flow3d simulation results are in reasonable agreement for this metric. Another important measure during the casting process is determining the length of the rods cast. Table 6 presents this information for the experimental measurements and simulation results with Flow3d. One can observe close agreement for the first two rods. The third rod showed a slight difference in the recorded lengths. This can be attributed to the partial fill of the first two rods where complete fill was not observed and caused some asymmetry in the distribution of mass of the melt and in the length of the third rod.

Table 6. Length of rods cast for 200 gm charge (in).

	INL Experiment	Flow 3d results	(Data-Sim)/Data
Rod 1	10	9.9	1%
Rod 2	10	9.6	4%
Rod 3	8.6	9.1	-6%

In an earlier paper extensive parametric analysis was performed to investigate the relative effects of each of the parameters surface tension, contact angle, and fluid viscosity on the casting problem. It was found surface tension had the most effect on the final solidification profile and the lengths of the rods cast. There was no validation data for the purely numerical results presented in the paper [1]. It was found that full fill of the rods was obtained when the Argon gas entrapment was ignored i.e. without the adiabatic model enabled for the single fluid model. Table 6 presents the lengths of the rods cast with the adiabatic bubble model so that effects such as rod breakage could be obtained. Both the results presented in Table 5 and 6 were obtained with surface tension specified as 0.20 N/m.

To demonstrate the transient casting process in Figure 6 we present transients as the melt flows down the casting apparatus at time 0.18 s and 1.8 seconds for the 200 gm simulation. Swirling flow phenomenon is visible in the inset of Figure 6. The complex evolutions of the transient VOF equation in three dimensions coupled with the Navier-Stokes equations provide the swirl in the flowfield. To demonstrate the swirling flow phenomenon the velocity vectors have been overlaid on the figure. In the first figure the molten charge just begins to fall under the effect of gravitational acceleration. The figure has been plotted with the color grading via the temperature field. After 1.8 s of simulation time no appreciable changes were observed in settling of the melt and it could be assumed that the casting part of the problem had reached steady state. The solidification process starts at the end of the flow settling down and subsequent cooling and phase change of the melt from molten state to solid state ensues.

Figure 7 presents the numerical simulations for rod 3 volume cast as a function of time prior to (while filling during casting) and after the solidification process. As can be observed from the figure much of the flow and settling down of the melt occurs before three (3 seconds) of simulation time.

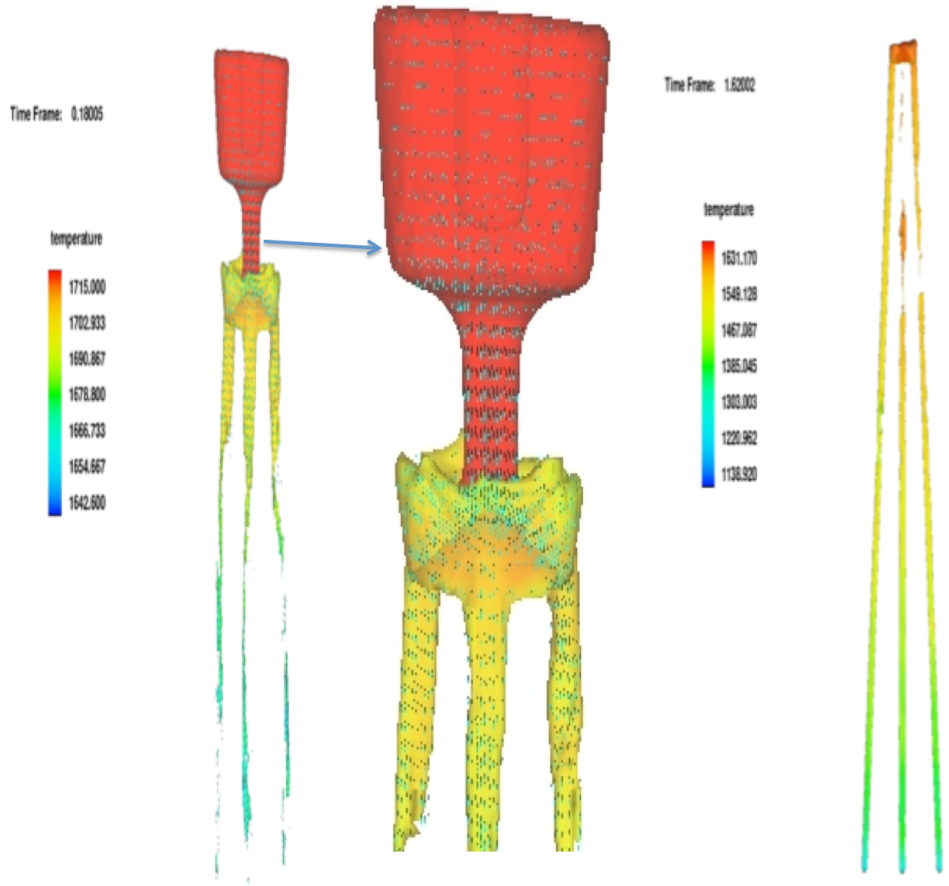


Figure 6. Transient casting simulation for 200 gm charge.

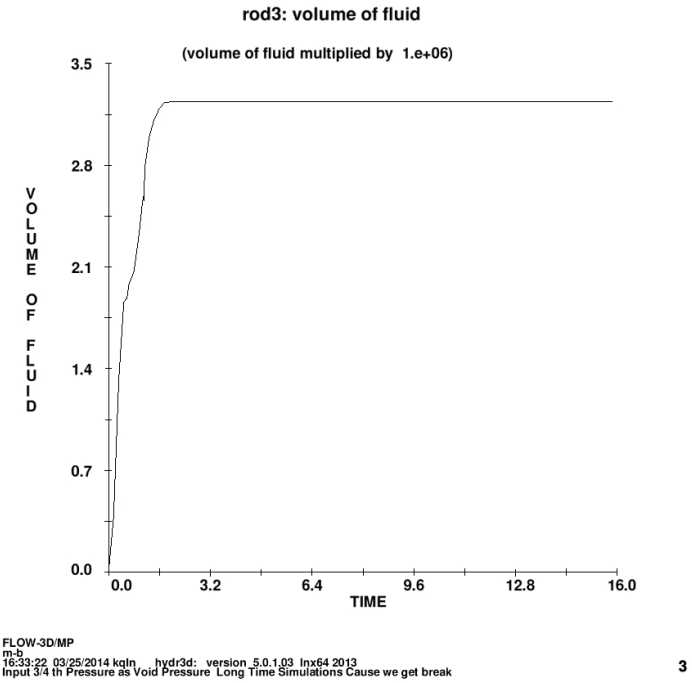


Figure 7. Predicted transient evolution of volume in rod1 (m^3) for 200 gm simulation.

Parametric Studies

We investigate the effects of key parameters that may affect the casting simulation. The effects of surface tension, wetting angle, and viscosity have been investigated as heuristic parameters earlier in a related study [1] and it was determined that surface tension plays a dominant role in determining the breakage pattern of the rods in the one fluid compressible fluid model. We investigate further effects of varying surface tension, valve discharge coefficient , and pressure inside the mold as parameters affecting the casting phenomenon in light of the experiments available.

a. Surface Tension Effects

Surface tension was taken initially at a nominal value of 1.50N/m. Parametric studies was performed by lowering this value to observe the effects on distribution of the rod volumes. It was observed that higher values of surface tension provide lesser breakup and a smoother flow down the casting apparatus. Thus this value of surface tension was used for presenting results.

Table 7: Length of rods (in) variation with surface tension (ST).

	INL Experiment	Flow 3d (ST-0.31)	Flow 3d (ST-0.20)
Rod 1	10.0	9.71	9.75
Rod 2	10.0	9.59	9.17
Rod 3	8.6	8.14	9.14

Table 7 presents the variation in the length of rods with surface tension for values of 0.31 N/m and 0.2 N/m respectively vs. the experimental data.

b. Presence of Valves

Each rod has a small vent hole at the bottom. We simulated the gas leakage from this vent using a valve component available in Flow3d. The mass flow rate, area of vent and the valve discharge coefficient are input to the valve model. The upper bound of the valve coefficient (the multiplication of the discharge coefficient and area) is estimated by assuming that volume in a rod can be discharge in casting time given in Figure 7 without any consideration of choked conditions.

Three cases are tested to study the effect of vent size; a- zero valve coefficient (no flow through vent), b- a valve coefficient of 1.78E-6, c-a valve coefficient of 3E-6 (simulating an effective increase in the area of the vent and discharge coefficient). In the simulations in addition to the low value of the discharge coefficient the vents close the instant the advancing front of the volume of fluid equation approaches the location of the vent. This further disallows the usage of vents for any significant differences in the flow behavior at steady state once they have come in contact with the advancing fluid front. The time taken for the melt to flow down the casting apparatus however was affected by the presence of vents. The time taken to reach steady state has been included in Table 8. The presence of the vent at the bottom significantly affected the filling time for the casting problem.

Table 8. Filling time for different valve coefficients.

	No Vent (nv)	$1.78x10^{-06}$ $m^{3.5}/kg^{0.5}$ (v1)	(nv-v1)/nv	$3.x10^{-06}$ $m^{3.5}/kg^{0.5}$ (v2)	(nv-v2)/nv
All Rods	1.65 s	1.32 s	-20%	1.21 s	-26.6%

As expected, a higher value of the valve coefficient resulted in a lower fill time of rods. Differing locations of the vents were not investigated since such studies have been performed earlier. Results of the change in the length of rods cast with increasing vent coefficients are provided in Table 9.

Table 9. Length of rods for varying valve coeffs (in).

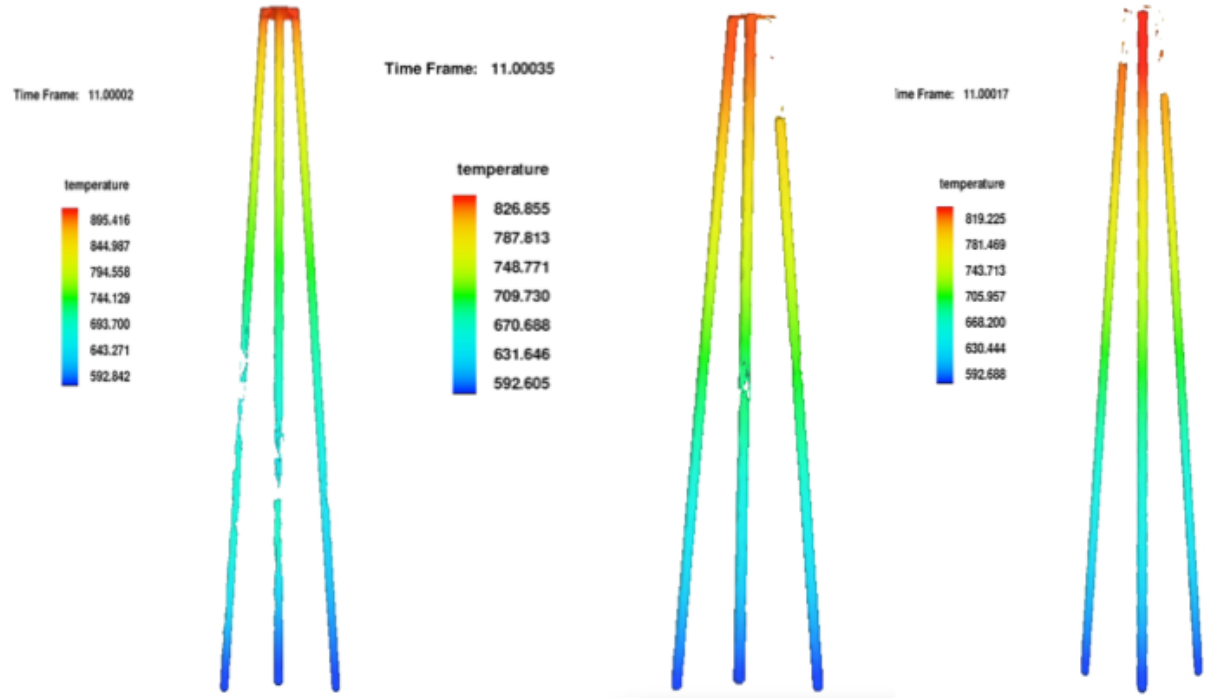
	No Vent (nv)	$1.78x10^{-06}$ $m^{3.5}/kg^{0.5}$ (v1)	(v1-nv)/nv	$3.x10^{-06}$ $m^{3.5}/kg^{0.5}$ (v2)	(v2-nv)/nv
Rod 1	9.56	9.78	+2 %	9.76	+2 %
Rod 2	9.04	8.96	-1 %	9.76	+8 %
Rod 3	8.10	8.77	+8 %	8.74	+8 %

From Table 9 we conclude inclusion of vents result in a more uniform rod distribution. Further with an increasing valve coefficient the lengths of the rods increased. To obtain an estimate of the relative volumes of the cast rods for the vent (v1,v2) vs. the no-vent (nv) cases we present the cast volumes in Table 10.

Table 10. Volume of rods with different valve coeffs ($x10^{-06}$ m^3).

	No Vent (nv)	$1.78x10^{-06}$ $m^{3.5}/kg^{0.5}$ (v1)	(v1-nv)/nv	$3.x10^{-06}$ $m^{3.5}/kg^{0.5}$ (v2)	(v2-nv)/nv
Rod 1	3.16	3.34	+6 %	3.41	+ 8 %
Rod 2	3.36	3.72	+11 %	3.55	+ 6 %
Rod 3	3.78	3.85	+2 %	3.95	+ 5 %

To obtain a better visual inspection of the volumes of the rods cast we present the final cast profiles for the cases where there is an absence of vent (nv) and with valve coefficients of $1.78x10^{-06}$ and $3x10^{-06}$ $m^{3.5}/kg^{0.5}$ in Figure 8.



(a) Plugged vent **(b) valc=1.78E-6** **(c) valc=3E-6**

Figure 8.: Final cast profiles for (a) Plugged Vent (c) Vent discharge coefficient= 1.78×10^{-06} $m^{3.5}/kg^{0.5}$ (c) Vent discharge coefficient= 3×10^{-06} $m^{3.5}/kg^{0.5}$.

As can be inspected visually the plugged vent case provides a final cast with a less uniform breakup of the rods as compared to the vented assembly (rod breakups at the lower part of caster are evident). The vented assembly provides for longer rod lengths with lesser breakup because there is an escape route for the gas from the assembly.

c. Pressure Variations

Another parameter that can be controlled while simulating the casting process is the initial pressure in the mold apparatus. To investigate the effect of pressure inside the mold cavity on the casting problem lower initial pressures were specified in the casting apparatus while performing simulations. Two different pressures of half (40 kPa) and three-fourth (60 kPa) of the initial pressure (from experiments) were specified initially as adjustable parameters inside the chamber prior to gravity pour. This simulates the real phenomenon where the pressure inside the actual casting chamber can be controlled externally to half and a quarter of the original pressure.

Table 11. Volume of rods variation distribution with pressure (x10^{-06} m^3).

	Flow 3d (80 kPa)	Flow 3d (60 kPa)	Flow 3d (40 kPa)
Rod 1	3.68	3.42	3.60
Rod 2	3.54	3.09	3.57
Rod 3	3.39	2.699	3.14

Table 11 presents the volume of rods cast with 60 kPa and 40 kPa pressures. A larger breakup of the rod was observed for the 60 kPa simulation compared to the 80 kPa simulation. The 40 kPa simulation did not exhibit any distinguishing flow features as compared to the 80 kPa simulation. Since the role of pressure is ill-defined in the transient Navier-Stokes equations and the second fluid Argon gas is only considered as a compressible fluid providing a pressure boundary condition it is difficult to draw conclusions based on the final cast profile with the pressure variations inside the chamber. Further, from the simulations it was realized that pressure fluctuations are considerable during transients and the overall the pressure variations do not affect the final cast of rods. This is further because of the quick temporal fluctuations of pressure during filling. In addition to the initial pressure in the chamber the presence of the bubble further adds complexity to the problem. The homogeneous Neumann boundary condition of no pressure variation in the normal direction to the surface of the bubble decides the overall pressure in the domain of the casting apparatus. The reasons of having different behavior at 40 and 60 Pa were not clear. Thus we performed further analysis by reducing the pressures to 25% and 12.5% of the initial pressures inside the mold apparatus. A summary of the rod volumes obtained for the analysis is provided in Table 12.

Table 12. Volume of rods variation distribution with pressure (x10^{-06} m^3).

	Flow 3d (20 kPa)	Flow 3d (10 kPa)	Flow 3d (5 kPa)
Rod 1	3.97	3.96	3.96
Rod 2	3.87	3.65	3.67
Rod 3	2.52	3.30	3.34

The second set of runs in Table 12 further establishes the assessment that transient pressure fluctuations vary rapidly and do not exhibit a conclusive effect on the volumes of the rods cast. If the flow problem provided slower settling times the cast rods could be affected by pressure variations. For the present case where settling occurs in a few seconds of the simulation time pressure does not affect the flow problem appreciably. In conclusion varying the pressure does not make any appreciable change in length or volume of the rods cast at the attainment of steady state. However the inclusion of vents significantly affects the time the flow problem takes to reach steady state. Increasing the vent coefficients also provided for a more uniform distribution of the rods and consequently larger rod lengths and less rod breakage.

d. Mesh Sensitivity

We performed a mesh sensitivity study for the problem with mesh refinement in each coordinate direction to twice the initial values. The initial mesh comprised of a total of 1.6 million cells (82 in x and y and 236 in z) yielding four elements along the diameter of the casting channels. A finer grid of 12.7 million elements that provided 164 elements along X and Y, and 472 in z was modeled to investigate the effect of grid size on the solution. A finer grid provides eight elements along the diameter of the casting channels. Temporal evolution of the flow problem as well as the final casting profiles for the finer mesh were compared with the coarse mesh. Mesh refinement does not affect the filling time for the rods noticeably. There is considerably more splashing with mesh refinement for the charge before it enters the mold cavity. The fill time however was not found to vary appreciably for either the coarse or fine mesh.

Table 13 presents the comparison of rod volumes that were determined for the mesh used in the analysis (Mesh1-m1) and the twice-refined mesh (Mesh 2-m2). The percent difference between the two mesh results with Mesh1 as the reference has also been provided. The maximum deviation in the results was found to be 7% between the two meshes. This can be considered negligible since the magnitude of the rod volumes is in the range of 10^{-06} m^3.

Table 13: Mesh sensitivity analysis for coarse and fine mesh ($x10^{-06}$ m^3)

	Mesh (Mesh1- m1) [82x82x236]	Finer Mesh (Mesh 2-m2) [164x164x472]	(m1-m2)/m1
Rod 1	3.96	3.66	-7 %
Rod 2	3.57	3.73	+4 %
Rod 3	3.41	3.35	+2 %

A parametric study was performed for longer time simulations on the temperature variations for the twice-refined mesh (Mesh 2) and the original mesh (Mesh 1). There were negligible differences in the temperature measurements through the transients. The sup (supremum) norm of temperature measurements were not found to vary not more than 1.2 °C-2 °C between the coarse and the fine mesh results. These differences can be considered negligible considering the range of temperature measurements from 580 °C-805 °C. The original mesh (82x82x236) results can be considered accurate for the temperature simulations. A similar convergence analysis was performed and the same conclusion was reached earlier in [1] when performing mesh sensitivity study.

Mesh of 82x82x236 cells (Mesh 1) utilized in the studies performed well on all the metrics of interest and provided accurate results. Further surface tension effects affect the casting problem appreciably and the correct value of this parameter was utilized in the modeling exercise to obtain results.

Swirling Flow

There are two possibilities for the occurrence of swirling flow. The first and demonstrable assumption is that swirling flow is a manifestation of the rich dynamics of the advancing front (interface) which evolves in time. The coupled volume of fluid equation (VOF) with the transient Navier-Stokes equations under the influence of gravity demonstrates complex flow structures with the evolving free surface in

three dimensions. Swirling flow in this case is a manifestation of the velocity components (u,v,w) that drive the advection equation for the VOF. Thus swirl in the flow is just the evolution of the explicit advected VOF field (in time) endowed with the velocity components obtained from the solution of the Navier-Stokes equations. This interpretation is more favored since we see the swirl in the advancing fronts in Figure 6 during the simulation. Since the flow has to fill the thin rods and they are the only passage the falling fluid has access to it is bound to exhibit a rich dynamics while flowing down.

The second interpretation of swirling flow could be that there are local turbulence effects while the melt is flowing down the casting apparatus. We modeled the melt as an incompressible fluid in the laminar regime without turbulence effects. The model performed well on capturing different aspects of the flow and the concomitant solidification problem. We conclude turbulence effects are thus small for this problem. We further highlight the complex flow metrics of the evolving interface already exhibit swirling phenomenon in three dimensions with laminar flow and turbulence effects are therefore not dominant.

The exiting of argon bubbles in the melt also has an effect on the turbulent behavior or the overall flow coming into rods. The counter-current melt-bubble can enhance the turbulent nature of incoming flow or cause or contribute to swirling. Regardless of the reasons, the observation from the velocity field indicate swirling in the entrance and in the upper part of the rods that support the designer reasoning to adding flow stabilizing groves at the bottom of the entrance region. The simulation of casting with these groves is in progress and will identify whether the groves will prevent swirling flow and provide flow directly into rods.

Conclusion

The U-Zr casting experiments performed at INL were simulated with Flow3D computer code. The goal was to develop a set of validated casting modeling parameters for the simulation of INL caster. Two different casting experiments of INL were simulated. The experimentally measured transient temperature profiles inside the casting apparatus were matched by adjusting primarily the heat transfer coefficients between melt and mold at different locations. Then parametric studies were performed to study the effects of changing pressures inside the mold, mesh refinements, surface tension effects, and presence or absence of valves at the bottom of the inner mold. Experimentally measured rod lengths, volumes and topographies were found to be in reasonable agreement with simulations. The validated model will be used in the simulation of larger size caster with larger outputs in the coming fiscal year.

Acknowledgements

This work was funded through the Fuel Cycle Research Development Project. The author would like to thank Dan Milano of Flow Science for his suggestions and guidance with some aspects of Flow3d simulations.

References

1. J. Crapps, D.S. Decroix, J.D. Galloway, D.A. Kozekwa, R. Aikin, R. Fielding, R. Kennedy, C. Unal. Separate effects identification via casting process modeling for experimental measurement of U-Pu-Zr alloys. Journal of Nuclear Materials 443 (2013) 176-184.
2. M.R. Barkhudarov, C.W. Hirt. Casting Simulation: Mold filling and solidification- Benchmark Calculations using Flow3d. Technical Report, Flow Science Inc.
3. R.W. Lewis, K. Ravindran. Finite element simulation of metal casting. International Journal for Numerical Methods in Engineering. 47 (2000), 29-59.
4. A. Kermanpur, Sh. Mahmoudi, A. Hajipour. Three dimensional Numerical Simulation of Metal Flow and Solidification in the Multi-cavity Casting Moulds of Automotive Components. International Journal of ISSI, Vol. 4 (2007), No. 1,2, pp. 8-15.
5. M.R. Barkudarov. Advanced simulation of the flow and heat transfer processes in simultaneous engineering. Technical Report, Flow Science Inc., 1998.
6. Flow-3d V10 User Manual, Version 10.0, in, Flow Science, Santa Fe, NM 2012.